Journal of
Materials Chemistry A

Accepted Manuscript

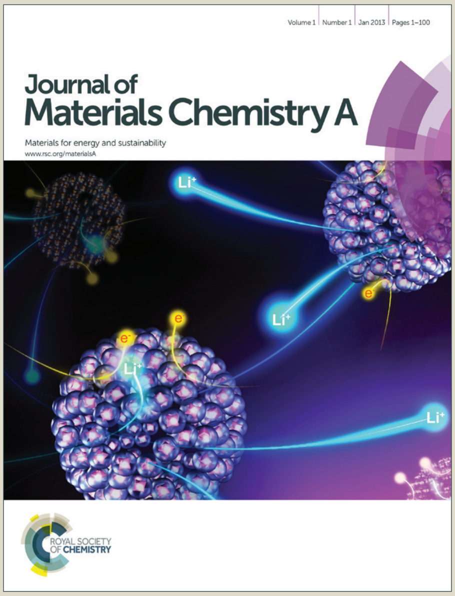

ROYAL SOCIETY
OF CHEMISTRY

www.rsc.org/materialsA

Tuning the structure and property of nanostructured cathode materials of lithium ion and lithium sulfur batteries

Gui-Liang Xu, Qi Wang, Jun-Chuan Fang, Yue-Feng Xu, Jun-Tao Li, Ling Huang and Shi-Gang Sun*

State Key Laboratory of Physical Chemistry of Solid Surfaces, Department of Chemistry, College of Chemistry and Chemical Engineering, Xiamen University, Xiamen 361005, China

Abstract

A large amount of progresses has been made to pursuit of high energy and high power battery devices in the past decades on account of the growing demand for clean and sustainable energy. The tremendous challenges in increasing the specific energy and power density of batteries lie mainly in the cathode materials. Lots of attempts have been made to improve the reversible capacity and rate capability of cathode materials for lithium ion batteries in the past few years. On the one hand, the rate capability of the cathode materials depends strongly on their surface structures, which determine the kinetics of lithium ion transportation and intercalation. Through tuning the surface structure of cathode materials, it can increase the density of channels for fast Li^+ diffusion, and therefore enhance greatly the surface/interfacial transportation kinetics of lithium ions; On the other hand, the reversible capacity of cathode materials of lithium ion battery is in direct proportion to the number of electron transferred, thus exploring high capacity cathode materials beyond intercalation such as sulfur cathode have been extensively conducted. The utilization efficiency of sulfur active materials, the reaction kinetics and trapping of soluble polysulfides depend also on the structure of sulfur cathodes. This review outlines recent developments on structure tuning of the most appealing cathode materials including layered lithium metal oxides, olivine structured $LiFePO_4$, spinel $LiMn_2O_4$ and $LiNi_{0.5}Mn_{1.5}O_4$, as well as sulfur cathodes. The structure-dependent properties of cathode materials are summarized mainly focusing on electrochemical performances, which can provide an in-depth understanding and rational design of high performance cathode materials. Further direction and perspective on research of the present field are also addressed.

Table of Contents (8cm*4cm, 20words)

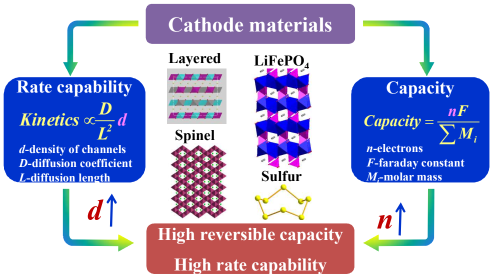

Recent progress and challenge on the structure design and electrochemical performances of layered cathode, $LiFePO_4$, spinel cathode and sulfur cathode.

Gui-Liang Xu received his Bachelor in July 2009 and Ph. D. degree in June 2014 from Department of Chemistry of Xiamen University under supervision of Prof. Shi-Gang Sun. He is now a post-doctoral fellow at Argonne national laboratory. He mainly focuses on the research of nanostructured materials for lithium ion batteries, Li/S and Li/O_2 batteries.

Shi-Gang Sun is a professor of chemistry at the State Key Laboratory of Physical Chemistry of Solid Surfaces, College of Chemistry and Chemical Engineering, Xiamen University, China. He received his Bachelor in 1982 from Xiamen University and Doctorat d'Etat in 1986 from Université Pierre et Marie Curie (Paris VI), and carried out one year post-doctoral research at the Laboratoire d'Electrochimie Interfaciale du CNRS, France. He is currently a Fellow of Royal Society of Chemistry, U.K., and a Fellow of International Society of Electrochemistry. His research interests include electrocatalysis, electrochemical surface science, spectroelectrochemistry, and electrochemical energy conversion and storage.

Yue-Feng Xu is currently a Ph. D. student at Xiamen University under supervision of Prof. Shi-Gang Sun. He received his Bachelor from Department of chemistry of Xiamen University in June 2012. His research interests are mainly focused on transition metal oxide electrode materials for lithium ion batteries.

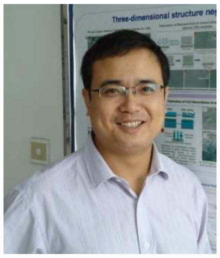

Jun-Tao Li received his Ph.D. degree from both Xiamen University and Université Pierre et Marie Curie in 2009. He is an associate professor at Energy Research School of Xiamen University, focusing on Interfacial study on electrochemical conversion and storage systems.

Ling Huang received his Ph. D. degree from Department of Chemistry of Xiamen University in 1997. He starts to work in Xiamen University from 2000 to date. He is now a professor of chemistry at Xiamen University, and his research interests include synthesis of tin based alloy by electrochemical deposition and high energy cathode materials of lithium ion batteries.

1. Introduction

The environmental pollution and global warming are extremely serious problems that we are facing in the twenty-first century.[1] In order to decrease the consumption of fossil fuel and emisssion of CO_2, the need for clean and sustainable energy is becoming more and more critical. As a result, the development of the next generation of energy-strorage mateials and devices have attracted extensive attention. Lithium ion batteries (LIBs), since its first commercialization by Sony Corporation in the early 1990s, have become the main power souces for portable electronics, and they are now showing great potential for the upcoming electrical vehicles (EVs) development.[2] However, the big challenge for applying the present LIBs is their low specifc energy as they react based on intercalation chemistry, in which the electron number invloved during the electrcochemical reaction is generally limited to one electron per formula.[3] In order to meat the demand of high energy and high power for EVs, one apporach is renewal of the present LIBs chemistry especially cathode materials.[4] The other way is to explore high energy batteries beyond intercalation.[5] Sulfur cathode, which differs from tranditional intercalation chemistry, can deliver ultra high specific capacity as high as 1675 mAh g^{-1} that is 5-10 times the specific capacities of tranditional intercalation cathodes.[6]

In this review, we will first focus on the progresses of nanostructured intercalation cathodes involving layered lithium metal oxide cathodes, olivine structured $LiFePO_4$ and spinel cathodes. The emphasis is mainly put upon the crystal habit-tuned synthesis and electrochemical behaviors of these cathode materials through tuning the surface/interfacial diffusion kinetics of lithium ions. Next, the main challenges and progresses of sulfur cathodes are summarized and discussed. Particular attention is given to the construction of nanostructured sulfur cathodes with fast diffusion paths of lithium ions and electrons, as well as good affinity for sulfur. Finally, a perspective and outlooks of further study along this direction are presented.

2. Crystal habit-tuned synthesis and electrochemical behaviors of nanostructured intercalation cathode materials

A typical lithium-ion battery is comprised of a layered lithium metal oxide cathode material and graphite anode material. They are separated by a porous membrane separator, which is soaked in a lithium-ion conducting electrolyte. It is also named as rocking-chair battery as the lithium ions “rock” back and forth between the cathode and the anode when the battery is charged and discharged. In the charging process, lithium ions are de-intercalated from the cathode, pass across the electrolyte and then inserted between the graphite layers in the anode, while electrons flow from the cathode to the anode through the external circuit (Figure 1).[7] This process is reversed in the discharging process. It can be clearly seen that LIBs operate based on the reversible shuttling of lithium ions between the cathode materials and the anode materials. As a consequence, the inherent properties of electrode materials will strongly restrict the performance of batteries.

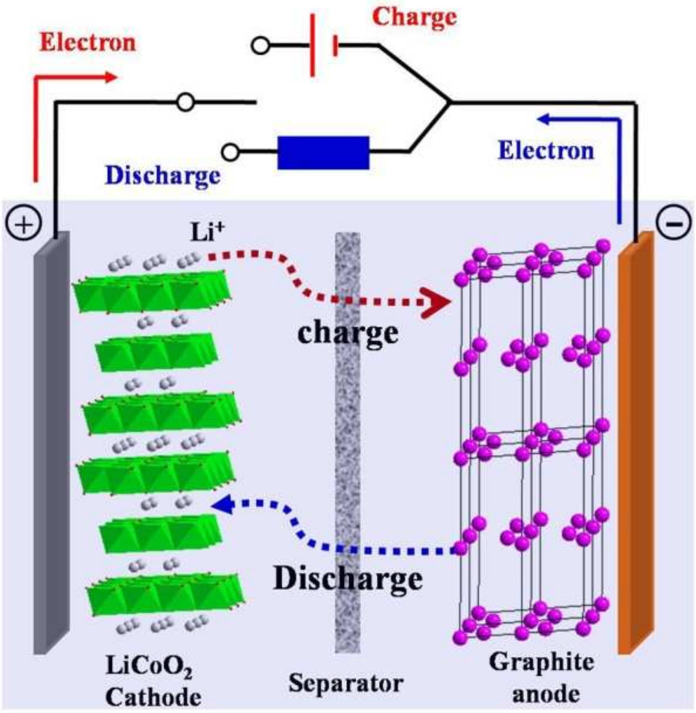

Figure 1 A scheme for working mechanism of lithium ion battery.

Compared to the anode materials, the cathode materials are the crucial factor that determines mainly the overall performance of batteries. The specific energy (*E,* Wh kg^{-1}) of a single battery cell can be calculated by the equation (Eq. 1) below,[8]

$$E=\frac{V_{cathde}-V_{anode}}{\frac{1}{C_{cathode}}+\frac{1}{C_{anode}}} \qquad \text{Eq. 1}$$

where C (mAh g^{-1}) represents the theoretical specific capacity and V (V) denotes the average working voltage. Generally, the specific capacity of anode materials exceeds largely that of the cathode materials, e.g. 372 mAh g^{-1} for graphite anode and only 170 mAh g^{-1} for $LiFePO_4$ cathode. Therefore, the specific energy of a single cell depends mainly on the specific capacity of cathode materials. As the cathode material of commercial LIBs, $LiCoO_2$ has a high theoretical capacity of 274 mAh g^{-1} and an average working voltage of 3.8 V (vs. Li/Li^+). However, in order to maintain its layered-structure, the upper potential of the de-lithiation for $LiCoO_2$ should be limited to 4.2 V, which means that only half of its theoretical capacity, i.e. 140 mAh g^{-1}, could be extracted.[9] When coupled the $LiCoO_2$ cathode with graphite anode, the single cell can only reach a practical specific energy of ~ 150 Wh kg^{-1} that is not sufficient to meet the growing demand for EVs application.

Extensive efforts have been made to explore alternative cathode materials with higher specific energy by increasing specific capacities or working voltage. Several lithium transition metal oxides have been considered as cathode materials in the past decades. Among them, oxides of a general formula $LiMO_2$ or $Li_2MnO_3 \cdot LiMO_2$ (M=Ni, Co, Mn) with layered structure,[10] $LiFePO_4$ with olivine structure,[11] $LiMn_2O_4$ and $LiNi_{0.5}Mn_{1.5}O_4$ with three-dimensional spinel structure[12] have been selected as the most promising cathode materials owing to their high working voltage and high specific capacities. However, they all face enormous challenges as a result of their inherent physical and chemical properties before they could be practically used. For example, the sluggish diffusion of electrons and lithium ions within layered cathode and olivine $LiFePO_4$ results in rapid capacity fading and inferior rate capability, while the electrochemical performances of spinel cathodes are very sensitive to the presence of Mn^{3+} ions and degree of cation order.

To overcome these problems and improve their electrochemical properties, considerable efforts have been made, such as surface coating[13] and fabrication of nano-sized particles.[14, 15] Nevertheless, the surface coating will decrease the overall specific capacity, and nano-sized particles tend to aggregate during repeated electrochemical charge/discharge process. As a result, the electrochemical performances cannot be significantly improved by these two strategies. It is widely reported that the structure of the battery materials, especially the surface structure plays a vital role on the rate for Li^+ insertion/extraction.[16] During the electrochemical charge/discharge process, Li^+ prefers to insert into the planes of open structure, such as {0110} facets of a layered lithium metal oxide cathodes with hexagonal crystal system,[17] (010) planes of olivine structured $LiFePO_4$ with orthorhombic crystal system[18] and (111) planes of Co_3O_4 with cubic crystal system.[19, 20] However, due to the isotropic growth of crystal seeds and the high surface energy of planes with open surface structure, irregular spherical particles are usually formed in a routine synthesis. Therefore, it needs to employ surface structure mediator during the preparation process in order to obtain single-crystals enclosed by single-crystalline facets. By tuning the crystal growth habit of nanoparticles, many regular morphologies such as nanorods, nanowires, nanoplates, octahedron, trioctahedron and tetrahexahedron were successfully synthesized through wet-chemical or electrochemical strategies, and showed significantly enhanced behaviors in energy storage and conversion systems.[21-24] Herein, we summarize systematically in this review the crystal habit-tuned synthesis and electrochemical performances of the most appealing intercalation cathode materials, including layered lithium metal oxide cathodes, olivine structured $LiFePO_4$ and spinel cathodes.

2.1 Surface structure tuning of layered lithium metal oxide cathodes and their enhanced electrochemical performances

2.1.1 Crystal structure analysis of layered lithium metal oxide cathodes

Layered cathode materials (LCM) including $LiNi_xCo_yMn_{1-x-y}O_2$ and

$xLiMn_2O_3 \cdot yLiMO_2$ (M=Ni, Co, Mn) have both been considered as one of the most appealing alternative cathode materials for the next generation LIBs owing to their high capacities.[25] However, the bulk layered cathodes suffer from rapid capacity fading and inferior rate property as a result of their sluggish diffusion kinetics of lithium ions. In the case of layered cathodes with α-$NaFeO_2$ structure, it was widely reported that Li^+ prefers to intercalate along the direction parallel to the Li^+ layers.[26] As illustrated in Figure 2a, the LCM presents a layered-structure with hexagonal crystal system, which can be described as layers of MO_6 (M= Co, Ni, Mn) octahedra alternatively stacked with layers of LiO_6 octahedra. Figure 2b shows the surface atomic structure of {0001} facets of LCM composing of NiO_6, CoO_6 and MnO_6 octahedra. These octahedra interconnect to each other by corner-sharing oxygen atoms and form a closely-packed structure, which will impede the transportation of Li^+ in the [0001] direction and hence lead to a low electrochemical activity of {0110} facets, because such closely-packed structure could not offer appropriate paths for Li^+ migration. In contrast to the {0001} facets, as shown in Figure 2c, the {0110} facets present an open surface structure of atomic arrangement, which could facilitate the migration of Li^+ between the MO_6 octahedra interlayers, and result in a high electrochemical activity. Based on the above analysis between the surface structures and the electrochemical properties, LCM electrodes with high percentage of {0110} facets will exhibit superior electrochemical performances.

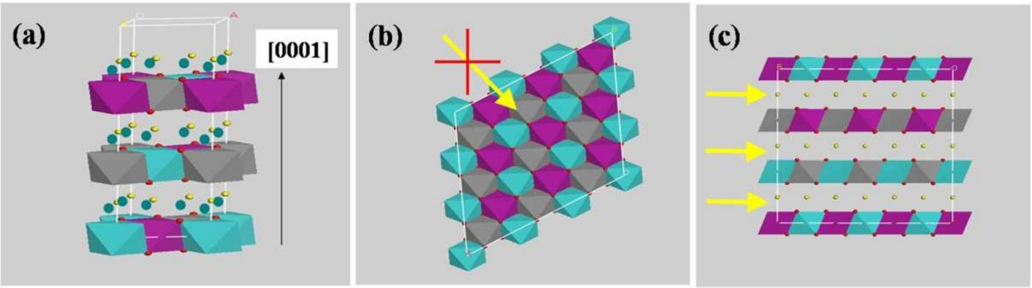

Bulk crystal structure {0001} facets {0110} facets

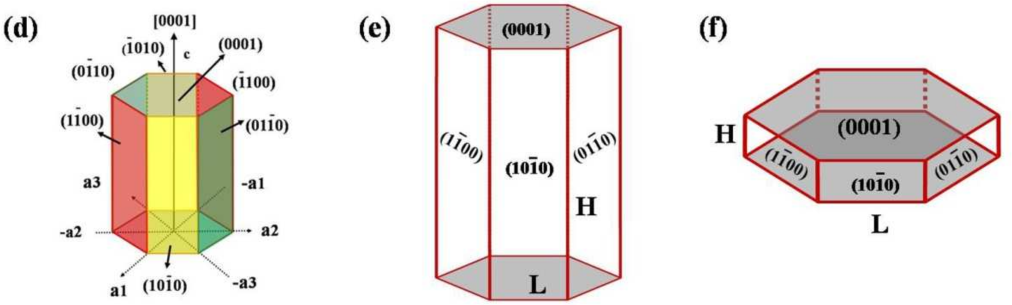

Figure 2 (a) Bulk crystal structure, (b) {0001} facets and (c) {0110} facets of layered cathode materials. (d) Miller-index assignment for crystals with hexagonal crystal system. (e) Crystal model grows along *c* direction (f) Crystal model grows along *a* direction. Reproduced with permission.[26] Copyright 2013 Royal Society of Chemistry.

Figure 2d represents a typical model of LCM crystal, and all the facets are indexed. The planes perpendicular to the *c* axis are assigned as (0001) planes. While the six-sided planes are indexed as $(01\bar{1}0)$, $(0\bar{1}10)$, $(10\bar{1}0)$, $(\bar{1}010)$, $(1\bar{1}00)$ and $(\bar{1}100)$, respectively, which are equivalent in a hexagonal crystal and all belong to the {0110} facets. Assuming its length and height are *L* and *H*, respectively, the geometrical areas and percentages of {0001} facets and {0110} facets in a perfect hexagonal crystal could be estimated by the equations below:

$$S_{\{0001\}} = 2\times(L\times\sqrt{3}L + 2\times\frac{1}{2}\times\sqrt{3}L\times\frac{1}{2}L) = 3\sqrt{3}L^2 \qquad \text{Eq.2}$$

$$S_{\{0110\}} = 6\times H\times L = 6HL \qquad \text{Eq.3}$$

$$S_{\{0110\}}\% = \frac{S_{\{0110\}}}{S_{\{0110\}}+S_{\{0001\}}} = \frac{6HL}{6HL+3\sqrt{3}L^2} = \frac{H/L}{H/L+\sqrt{3}/2} \qquad \text{Eq.4}$$

It is obvious that a big value of the *H/L* ratio will lead to a high percentage of

{0110} facets. Figure 2e illustrates the crystal model of LCM growing along *c* direction. The *H/L* value will be increased with the increase of *H*, resulting in a high percentage of {0110} facets. While if the LCM grows long *a* direction (Figure 2f), a low percentage of {0110} facets could be estimated as the *H/L* value will be greatly decreased. Therefore, with the purpose of developing LCM electrodes with high percentage of {0110} facets, the LCM electrodes had better grown along the *c* direction. As a result, the percentage of {0110} facets will increase successively on hexagonal sheets, hexagonal nanobricks, hexagonal nanoprisms, nanorods and nanowires as illustrated in Figure 3.

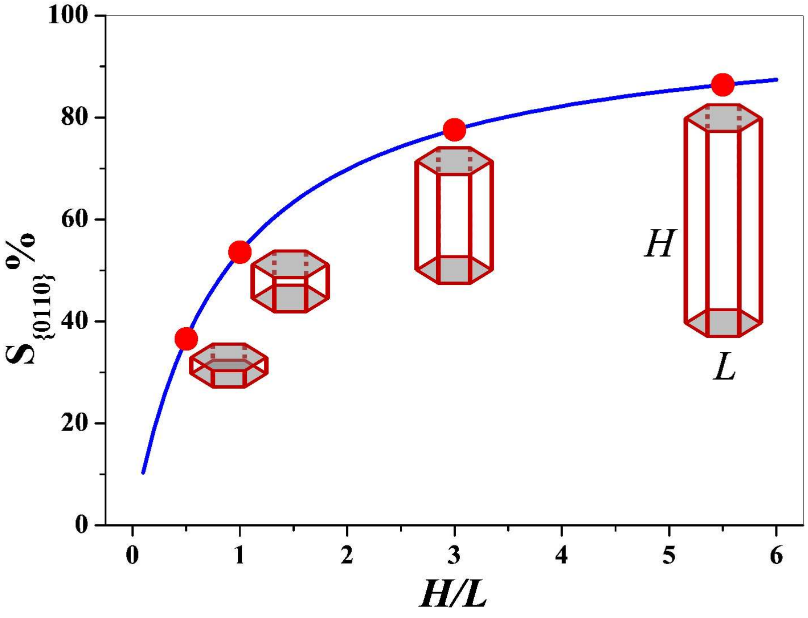

Figure 3 Percentages of {0110} facets as a function of *H/L* for different LCM nanostructures.

2.1.2 Crystal habit-tuned synthesis of LCM with high percentage of {0110} facets and their electrochemical properties

In this section, we will particularly focus on the progress of the surface structure tuning of layered $LiNi_xCo_yMn_{1-x-y}O_2$ and $xLi_2MnO_3{\cdot}yLiMO_2$ (M=Ni, Co, Mn) cathode materials with high percentage of {0110} facets. As a result of the high surface energy of {0110} facets, it needs to explore new synthetic strategy that can break the restriction of thermodynamics that requires the minimization of total surface energy, resulting in a diminution of the total surface energy of nanocrystals enclosed with high surface energy facets during their growth.[10] The method of using a surface-structure agent such as poly(vinylpyrrolidone) (PVP), oxalate acid or polyol medium to selectively adsorb or stabilize the crystal facets of metal hydroxides or metal oxides precursors, and following by high temperature calcination with lithium salts is one of the most reported strategies. Two dimensional structures (2D), one dimensional structures (1D) and hierarchical micro/nanostructures of layered cathode materials were successfully synthesized through different synthetic approaches.

2D nanostructures. Many studies have demonstrated that 2D nanostructured electrodes present excellent lithium storage performance in the past decades.[27-29] 2D $LiNi_xCo_yMn_{1-x-y}O_2$ and $xLi_2MnO_3{\cdot}yLiMO_2$ (M=Ni, Co, Mn) such as nanosheets, nanoplates and nanobricks were successfully synthesized and showed enhanced rate capability. Lots of synthetic approaches were employed to synthesize metal hydroxides and metal oxides precursors with deliberately designed nanostructures including co-precipitation, solvothermal reaction and hydrothermal reaction. The surface-structure mediators that induced during the preparation process have great influence on the resulted morphologies. By co-precipitation method with PVP as surface-capping agent, Fu and co-workers [26] synthesized single-crystalline $LiNi_{1/3}Co_{1/3}Mn_{1/3}O_2$ (LNCM) hexagonal nanobricks with a percentage of 58.6% for {0110} facets. The synthesis process can be approximately divided into two stages: (1) adsorbate-directed synthesis of the $Ni_{1/3}Co_{1/3}Mn_{1/3}(OH)_2$ nanosheets, and (2) growth of $Ni_{1/3}Co_{1/3}Mn_{1/3}(OH)_2$ nanosheets to LNCM nanobricks.[26] In this study the PVP functioned as a structure-directing agent for the growth of $Ni_{1/3}Co_{1/3}Mn_{1/3}(OH)_2$ nanosheets, and adsorbed on negatively charged {0001} facets via the amine groups through electrostatic interaction. As a consequence, the growth rate of the [0001] direction was decreased, and led to the formation of {0001}-dominated $Ni_{1/3}Co_{1/3}Mn_{1/3}(OH)_2$ nanosheets. After pre-calcination at 450 °C, the PVP was decomposed and lithium ions were gradually inserted into the $Ni_{1/3}Co_{1/3}Mn_{1/3}(OH)_2$. Along with rising the calcination temperature, Li^+ was continuously inserted into the interlayers of $Ni_{1/3}Co_{1/3}Mn_{1/3}(OH)_2$ along the [0001] direction, causing the formation of LNCM hexagonal nanobricks. By analyzing their surface structures using TEM and SAED, it was found that the frontal planes of the as-prepared nanobricks were enclosed by {0001} facets, while the lateral planes were enclosed by {0110} facets (Figure 4a and c). It was obviously observed that the {0001} facets present closely-packed structure while the {0110} facets exhibit open surface structure from the HRTEM images (Figure 4b and d), which were in accordance with their surface atomic arrangement models, respectively. The electrochemical test results showed that the LNCM nanobricks exhibit excellent rate capability owing to the increased percentage of {0110} facets, which can facilitate the transportation of lithium ions. The initial discharge capacities at rates of 2, 5, 10 and 15 C-rates were determined at 159.1, 151.3, 136.1 and 130 mA h g^{-1}, respectively. Their capacity retentions after 100 cycles were retained at 89% (2 C), 91.2% (5 C), 93.5% (10 C) and 91.9% (15 C), respectively (Figure 4e). The result demonstrated also that it present higher rate capability with increasing lateral thickness of the nanobricks (Figure 4f), ascribed to the higher percentage of {0110} facets as the nanobricks growing along *c* direction.

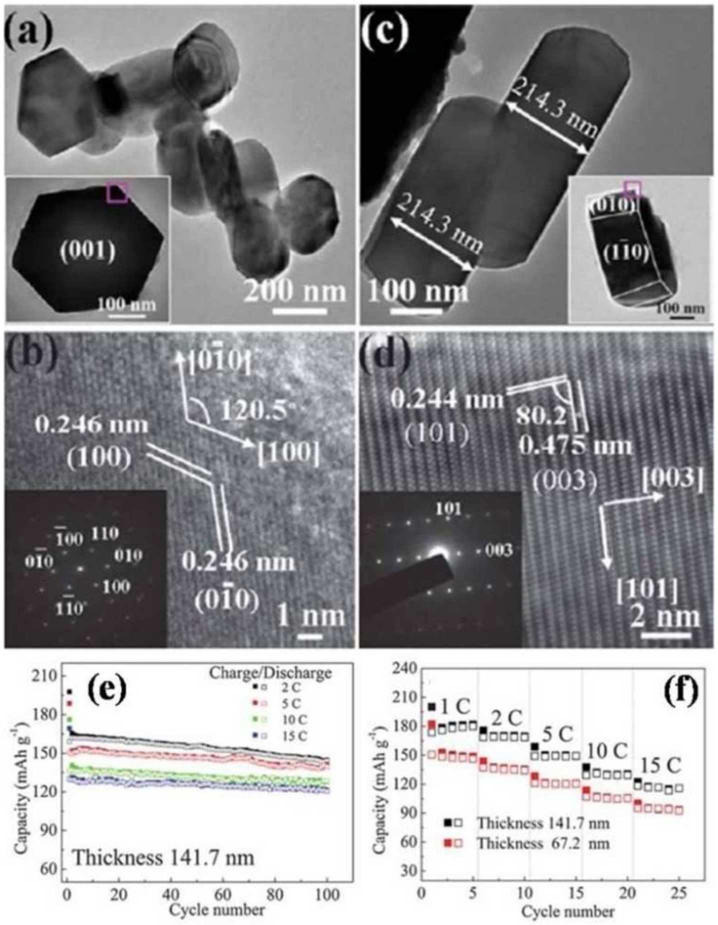

Figure 4 (a) TEM images of the frontal view of LNCM nanobricks. (b) HRTEM image and SAED pattern of the frontal plane of a single nanobrick shown in (a). (c) TEM images of the lateral view of LNCM nanobricks. (d) HRTEM image and SAED pattern of the lateral plane of a single nanobrick shown in (c). (e) Cycling performance of LNCM at different charge/discharge rates. (f) Comparison of the rate capability of the nanobricks with different sidewall thickness. Reproduced with permission.[26] Copyright 2013 Royal Society of Chemistry.

Similar result was recently reported by Cao and co-workers [30], in which they prepared LNCM nanoplates with {0110} facets exposure in polyol medium. Ethylene glycol played an essential role, which served as solvent and chelating reagent simultaneously. A plate-like structure was formed benefiting from the hydrogen bond and chelating effects of ethylene glycol. The results indicated also that the percentage of {0110} facets can be increased as increasing the thickness of LNCM nanoplates, resulting in more diffusion channels for Li^+. The LNCM nanoplates calcined at 850 ºC for 12 h (LNCM-850-12H) can deliver an initial discharge capacity up to 207.6 mAh g^{-1} at 20 mA g^{-1}, and the discharge capacities were retained at 169.8, 160.5 and 149.3 mAh g^{-1} at rates of 2, 5 and 7 C, respectively, demonstrating superior rate capability. The excellent electrochemical properties of the LNCM-850-12H were ascribed to the high percentage of {0110} facets. Besides, $LiCoO_2$ nanoflakes[31] and $LiNi_{0.5}Mn_{0.5}O_2$ nanosheets[32] with increased {0110} active facets were also reported and showed remarkable improvements on their specific capacity and rate property compared to their bulk materials, which both resulted from increased surface/interfacial diffusion kinetics of lithium ions. However, it is worthwhile noted that $LiCoO_2$ nanoplates with exposed {0001} facets and high rate capability was also reported by Li and co-workers, [33] such $LiCoO_2$ nanoplates can maintain a stable reversible capacity of around 120 mAh g^{-1} in 100 cycles at 7 C. But the excellent rate property of the as-prepared $LiCoO_2$ nanoplates was attributed to the many cracks on the nanoplates, which were perpendicular to the {0001} facets. According to the crystal structure characteristics of LCM, these cracks may be enclosed by the high electrochemically active {0110} facets and can hence favor the diffusion of Li^+.

In the study of 2D Li-rich layered cathode materials, the surface energy for the main planes of the $Li(Li_{0.17}Ni_{0.25}Mn_{0.58})O_2$ (LNMO) were firstly calculated with the help of the Vienna *ab* initio simulation package (VASP) by Wei et al.[17] The calculation result indicated that the surface energy of the {0110} facets was 1.467 J m^{-2} (Figure 5a), which was higher than that of the {0001} facets (0.937 J m^{-2}). As the growth rate of high-energy facets is faster than that of low-energy facets, the high-energy facets tend to disappear during growth and the surface of the grown crystal will be mainly enclosed by low-energy facets.[16] Therefore, the {0001} dominated nanoplates were thermodynamic equilibrium products in a routine synthetic procedure. Wei and co-workers [17] demonstrated that a different precursor and a shorter hydrothermal time both enabled the nanoplates growing simultaneously in the [0110] and [0001] direction, leading to the formation of {0110} facets dominated nanoplates in comparison with the conventional nanoplate material (Figure

5b, c, d and e). The electrochemical results illustrated that the {0110} facets dominated LNMO nanoplates exhibited a superior rate property with a high reversible capacity. A reversible capacity up to 186 mAh g^{-1} after 50 cycles at a high charge/discharge rate of 6 C-rate could be recovered (Figure 5f). While the conventional LNMO nanoplates and LNMO particles released only 106 mAh g^{-1} and 40 mAh g^{-1} after 50 cycles at the same rate. The outstanding rate capability was ascribed to the increased diffusion channels for fast Li^+ intercalation/de-intercalation on the {0110} facets dominant nanoplate materials.

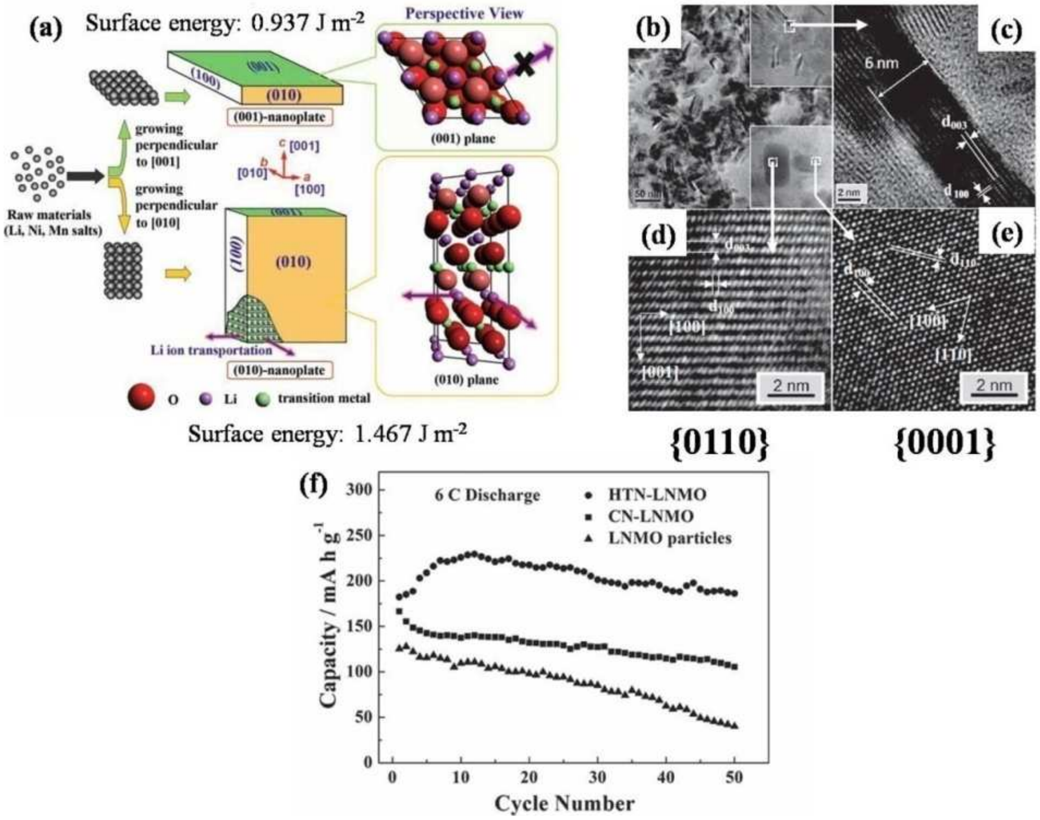

Figure 5 (a) Schematic illustration of two kinds of nanoplates and the microstructure of their surfaces. (b, c, d and e) TEM characterization of the crystal habit-tuned LNMO. (f) Discharge capacity at a 6 C-rate of (1) LNMO particles, (2) conversional nanoplate-LNMO and (3) crystal habit-tuned nanoplate-LNMO. Reproduced with permission.[17] Copyright 2010 Wiley-VCH.

1D nanostructures. According to the above structural analysis, with the LCM continuously grows along *c* direction forming 1D nanostructures such as nanorods and nanowires, the *H/L* value will be further increased, corresponding to higher percentage of {0110} active facets. Moreover, 1D structure could accommodate the volume variation in its radial direction and facilitate the diffusion of lithium ions and electrons in its axial direction.[34-42] However, it is very difficult for 1D nanostructures to preserve their original structure under high temperature calcination during the preparation of LCM. 1D metal oxides or metal hydroxides precursors were destroyed and transformed into irregular nanoparticles after high temperature calcination in the previous studies.[43] As a consequence, novel synthetic strategy or more preciously controlled reaction conditions are therefore required.

Kim and co-workers [44] reported spontaneous growth of $Li[Ni_{0.25}Li_{0.15}Mn_{0.6}]O_2$ nanowires via a hydrothermal method at 200 °C for 5 h. $Ni_{0.3}Mn_{0.7}O_2$ precursor was prepared firstly, which was synthesized through ion-exchange reaction of $K_{0.32}MnO_2$ with $NiCl_2{\cdot}2H_2O$ in aqueous solution at room temperature for 5 days. The anisotropic reactivity of the surfaces and the high chemical-potential environment played a key role in the highly preferential growth along a specific direction, which were created by the release of the stored energy in the pre-nucleated metastable phase during heating at the appropriate temperature.[44] Figure 6a and c depict the SEM and TEM images of the $Li[Ni_{0.25}Li_{0.15}Mn_{0.6}]O_2$ nanowires that could be obtained with lengths over 1 mm and diameters of ~ 30 nm. The HR-TEM image (Figure 6b) illustrates the d-spacing value that was measured at 0.47 nm, corresponding to the lattice distance of the (003) plane of the layered cathode materials. Combining the open rather than closely-packed atomic arrangement from the HRTEM image, it can draw conclusion that the as-prepared nanowires may grow along the *c* direction, suggesting that the nanowires are mainly exposed with {0110} facets. Figure 6d illustrates the cycle performance of $Li[Ni_{0.25}Li_{0.15}Mn_{0.6}]O_2$ nanowires at 0.3 C-rate (1 C=400 mA g^{-1}) with a voltage range of 2-4.8 V. It delivered an initial discharge capacity as high as 311 mAh g^{-1} with an initial coulombic efficiency up to 85%. A reversible discharge capacity of 294 mA h g^{-1} could be still maintained after 80 cycles, corresponding to a high capacity retention of 95%. In addition, the TEM image (Figure 6e) of $Li[Ni_{0.25}Li_{0.15}Mn_{0.6}]O_2$ nanowires electrode after 80 cycles indicates a well conservation of the 1D nanowire structure. Figure 6f further indicates that the as-prepared nanowires present a much better rate capability than the nanoplate material. At a high rate of 7 C, it can still deliver a discharge capacity of 256 mA h g^{-1}. The greatly enhanced electrochemical performance of $Li[Ni_{0.25}Li_{0.15}Mn_{0.6}]O_2$ nanowires could be attributed to the significantly increased {0110} facets for the nanowire crystallographic texture, which could significantly enhance the surface/interfacial diffusion kinetics of lithium ions. Besides the $Li[Ni_{0.25}Li_{0.15}Mn_{0.6}]O_2$, $LiCoO_2$ nanowires[45] were also synthesized by Li and co-workers, in which cobalt precursor $Co(CO_3)_{0.35}Cl_{0.2}(OH)_{1.1}$ nanowire bunches precursor was firstly prepared through hydrothermal reaction, and then turned into Co_3O_4 nanowires by further heat treatment at 500 °C for 3 h. The HR-TEM image illustrated that the $LiCoO_2$ nanowires consist of nanoparticles, which were mainly enclosed by {0110} facets. The resulted $LiCoO_2$ nanowires demonstrated both outstanding cycleability and rate capability, in which a reversible capacity of 100 mAh g^{-1} at 1 A g^{-1} after 100 cycles was maintained. The enhanced electrochemical properties of the $LiCoO_2$ nanowires may be attributed to their 1D nanostructure and the exposure of {0110} facets, as the {0110} facets exhibit high electrochemical activity for layered $LiCoO_2$ and can enable fast Li^+ transportation.

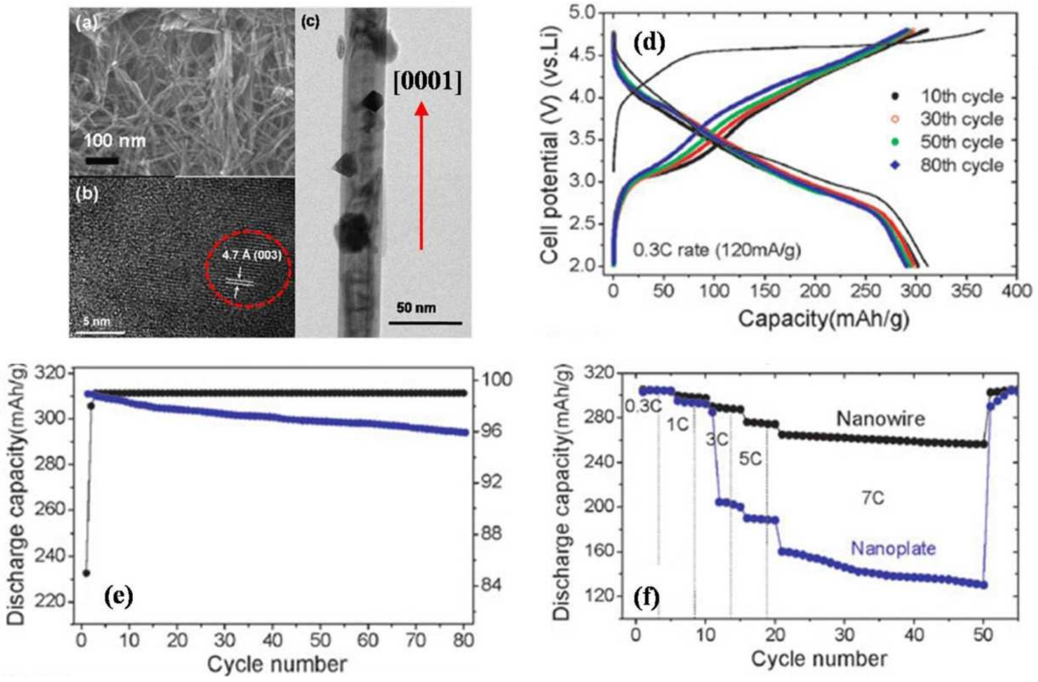

Figure 6 (a) SEM, (b) HRTEM and (c) TEM images of the Li[$Ni_{0.25}Li_{0.15}Mn_{0.6}$]$O_2$ nanowires. (d) Plot of cycle life and coulombic efficiency of the nanowires as a function of the cycle number at a rate of 0.3 C-rate (=120 mA g^{-1}). (e) TEM image of the Li[$Ni_{0.25}Li_{0.15}Mn_{0.6}$]$O_2$ nanowires electrode after 80 cycles. (f) Rate capabilities of the nanowires and nanoplates with the Li[$Ni_{0.25}Li_{0.15}Mn_{0.6}$]$O_2$ composition at different C-rates. Reproduced with permission.[44] Copyright 2009 Royal Society of Chemistry.

Hierarchical micro/nanostructures. Another critical issue of nanostructures with high electrochemically active facets is their tap density that greatly determines their volumetric energy density. Hierarchical micro/nanostructures that are composed of primary nanoparticles were therefore developed, which could bring advantages of synergistic effects of primary nanoparticles and secondary nanostructures. Recent studies were mainly focused on the construction of hierarchical micro/nanostructured LCM with the primary units enclosed by the high electrochemically active facets and assembled into micro-sized secondary structures. Co-precipitation was proved to be an effective method to construct hierarchical micro/nanostructures through fine controlling experimental conditions. Zhou and co-workers[46] reported mono-dispersed $Li_{1.2}Mn_{0.6}Ni_{0.2}O_2$ microspheres consisting of primary nanoplates, and found that the pH value during the co-precipitation process play a critical role in determining the thickness and the packing style of the primary nanomaterials. By adjusting the pH value from 9.0 to 11.0, these primary nanomaterials presented closely-packed plates, then well exposed nanoplates, and finally they turned into nanoparticles, respectively. Further calcination of the precursors with Li_2CO_3 produced lithium-rich layered $Li_{1.2}Mn_{0.6}Ni_{0.2}O_2$ cathode materials with well conservation of the morphology of the hydroxide precursors. Among the above three different samples, due to the uniform particle size distribution and the shortened Li^+ transportation paths, the one assembled from well-exposed primary nanoplates possessed excellent rate capability and satisfactory cycling stability. Wang and co-workers[47] prepared nano-architectured $Ni_{0.25}Mn_{0.75}(OH)_2$ precursor by optimizing experimental conditions during the co-precipitation process, which was assembled from hexagonal shaped nanoplates. After heat treatment with the lithium salts at 900 °C, the nanoplates developed rounded edges, shrunk in lateral dimension, and expanded in thickness, leading to a decrease in the non-electrochemically active {0001} facets. The resulted $Li_{1.5}Ni_{0.25}Mn_{0.75}O_{2+d}$ cathode material could maintain 275 mAh g^{-1} up to 50 cycles at a rate of 0.1 C-rate and still 159 mAh g^{-1} at 5 C-rate, illustrating superior cycle and rate performance. Sun and co-workers [48-50] synthesized a series of concentration gradient layered Li-Ni-Mn-O cathode materials using continuously stirred tank reactor (CSTR), in which the Mn concentration remained constant throughout the particle, while the Co concentration increased and the Ni concentration decreased linearly from the center to the outer surface of the particle. The as-prepared FCG-Mn-F material presented an average composition of $Li[Ni_{0.60}Co_{0.15}Mn_{0.25}]O_2$ and was comprised of rod-shaped primary particles, whose length reached 2.5 μm and grew in its radial direction (Figure 7a). According to the crystallology, the facets parallel to *a* direction and *c* direction should be {0110} facets, which are active facets for layered cathode materials. Therefore, in addition to the full concentration gradient, it is believed that the primary nanorods with crystallographic texture play an important role on its enhanced rate property and increased low temperature performance in comparison with conventional composition (CC) $Li[Ni_{0.60}Co_{0.15}Mn_{0.25}]O_2$ (Figure 7b).

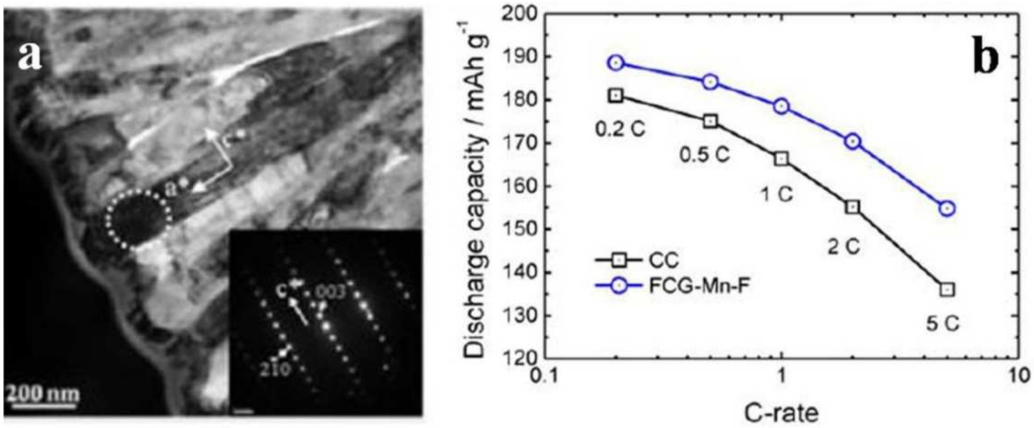

Figure 7 (a) TEM image and the corresponding electron diffraction pattern from FCG–Mn-F primary particle. (b) Rate capabilities of CC and FCG-Mn-F $Li[Ni_{0.60}Co_{0.15}Mn_{0.25}]O_2$ cathodes. Reproduced with permission.[49] Copyright 2013 American Chemical Society.

Therefore, by crystal habit-tuned synthesis of layered cathode materials and using surface structure mediator, it can break the thermodynamic limitation and prepare nanomaterials with high percentage of {0110} on active facets. Owing to the enhanced surface/interfacial diffusion kinetics of lithium ions, they all demonstrated improved rate capability with higher reversible capacity in comparison with their bulk materials. Consequently, the surface structure tuning offers a novel strategy to enhance the electrochemical performances of cathode materials. However, there is one point need to be notified. The transportation paths of lithium ions inside the LCM bulk crystal during charge/discharge process are very complex. Ceder et al. reported that lithium is coordinated octahedrally by oxygen atoms but diffuses from site to site by hopping through intermediate tetrahedral sites.[51, 52] They demonstrated that the combined use of low-valent transition-metal cations and low strain in the activated state are key strategies to enhance the rate capability of the electrode materials.[53] While what we focus on in this review is to tune the surface/interfacial diffusion paths of lithium ions, which seems opening a door for the transportation of lithium ions from the surface to the bulk crystal and may decrease Li diffusion energy and can therefore enhance the transport kinetics, resulting in further improving the specific capacity and rate capability of cathode materials.

Another strategy to improve the specific capacity and rate capability of layered cathode is to modify their interlayer distance and the interaction forces between the adjacent layers, which was confirmed in the case of layered V_2O_5 cathode material,[54-56] and is also an efficient approach to optimize their electrochemical performances in addition to surface structure tuning. However, there is little work on tuning the interlayer distances of layered lithium transition metal oxide cathodes so far.

2.2 Surface structure tuning of $LiFePO_4$ cathode materials and their enhanced electrochemical performances

The facet-dependent properties of $LiFePO_4$ (LFP) cathode materials were also investigated by experimental evidence and theoretical calculation. Since firstly reported by Padhi et al. in 1997,[57] LFP cathode materials in olivine structure have attracted extensive attention due to its high theoretical specific capacity (170 mAh g^{-1}), relatively high charge/discharge voltage plateau of 3.4 V (vs. Li/Li^+), long cycle stability, low cost and toxicity, high safety, as well as its one dimensional diffusion channels along [010] direction.[18, 58-60] Owing to the above merits, LFP has been considered as one of the most appealing cathode alternatives for the dynamic batteries used in EV and HEVs. In the past few years, considerable attempts were made to enhance their electrochemical performances by construction of LFP nanomaterials with open surface structure of (010) planes. In this section, the development of surface structure tuning on LFP cathode materials and their enhanced electrochemical properties are summarized.

2.2.1 Crystal structure analysis of LFP

Olivine LFP presents an orthorhombic lattice structure with the space group of Pnma. The lattice parameters are a=1.0329 nm, b=0.6006 nm, c=0.4691 nm, and V=0.2910 nm^3. In a typical crystal structure of LFP (Figure 8a), the divalent Fe^{2+} ions occupy the corner-shared octahedra, the P^{5+} is located in tetrahedral sites, and Li^+

resides in chains of edge-shared octahedra. However, the corner-shared FeO_6 octahedra are separated by the oxygen atoms of the PO_4 tetrahedra and cannot form a continuous FeO_6 network, resulting in a poor electronic conductivity of LFP.[11] Extensive efforts, including carbon coating, incorporating LFP with highly conductive materials, metal ions doping and fabrication of nano-sized particles were all used to enhance the electrochemical performance. While Ceder and Kang reported that a rate capability equivalent to full battery discharge in 10-20s can be achieved by creating a fast ion-conducting phase through controlled off-stoichiometry.[61] On the other hand, tuning the surface structure of LFP cathodes has been demonstrated to be an effective approach to enhance its rate capability, and thus attracted lots of attention in the past few years.

Many theoretical calculations and atomistic modeling were applied to study the surface energy and structure, and their relevance to the electrochemical behaviors. Figure 8b, c and d show the surface atomic structures of (010), (001) and (100) planes, respectively. 1D diffusion channels for lithium ions could be obviously observed in the (010) planes and (001) planes of LFP. Ceder et al.[62] firstly studied the Li^+ transport in olivine LFP by the first-principle calculations. The results indicated that the (010) planes possess a lower Li migration energy and higher Li diffusion coefficient up to several orders of magnitude than (001) planes. This result was also confirmed by Islam and co-workers using well-established atomistic modeling techniques.[63, 64] Ceder et al.[65] further illustrated that Li redox potential on the (010) planes is 2.95 V, which is much lower than the bulk value of 3.55 V. Therefore, given the highly anisotropic nature of LFP, maximizing the exposure of (010) planes over others would be an effective approach to optimize the rate capability. Figure 8e presents a typical crystal model of LFP with orthorhombic crystal system, and the main crystal planes are indexed. According to the above theoretical analysis, the LFP nanocrystals had better grown along *ac* plane, forming (010) planes dominated nanoplates or 1D nanostructures, as illustrated in Figure 8f. However, Nazar and co-workers[66] pointed out that the actual activation energy for hoping should be much higher in the presence of strong binding to the lithium ions than that obtained by first principles calculation, since their models assumed no interaction of the polarons with the lattice. While Maier and co-workers[67] found that the order of magnitudes for ionic conductivity and the diffusion coefficient in both the (010) and (001) planes are the same at ~ 150 °C. Despite this, various LFP nanomaterials with exposed (010) planes, including nanoplates, nanorods and nanowires were synthesized by different methods and indeed showed dramatically improved electrochemical performances with solid experimental evidences, indicating a large benefit of the open surface structure of (010) planes on the enhanced electrochemical performances of LFP.

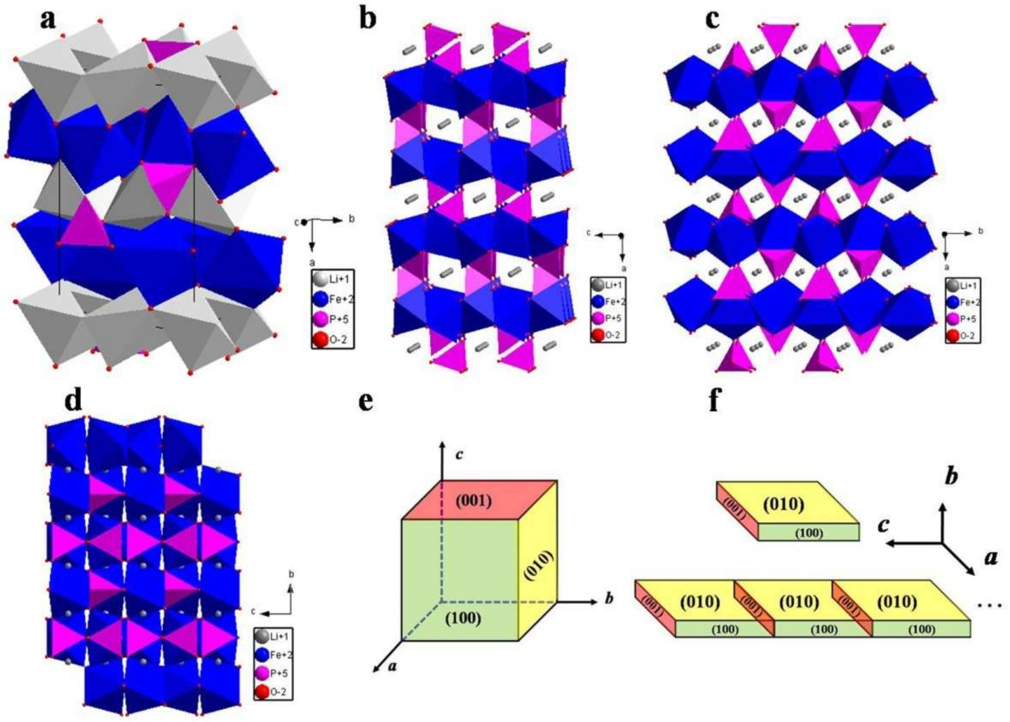

Figure 8 (a) Crystal structure of bulk LFP and surface atomic arrangements for different crystal planes of LFP: (b) (010) planes, (c) (001) planes and (d) (100) planes. (e) Miller-index assignment for LFP with orthorhombic crystal system. (f) Crystal models of LFP growing along *ac* plane.

2.2.2 Crystal habit-tuned synthesis of LFP cathode materials and their electrochemical performances

LFP nanoplates. In the past few years, lots of work were done to prepare LFP nanoplates with (010) planes exposing through various synthetic routes, such as solvothermal,[68] hydrothermal,[69] co-precipitation,[70] microwave-assisted,[71] solid-state reaction,[72] liquid-phase reduction,[73] supercritical fluids synthesis.[74] Among them, hydrothermal reaction and solvothermal method are two of the most employed strategies. By adjusting the reaction temperature, reaction time, concentration and composition of surfactants, the structures of LFP could be well controlled.

Wang et al. [68] reported two kinds of olivine LFP nanoplates synthesized by solvothermal reaction in glycol medium, in which the dominated crystallographic plane of the LFP nanoplates and the corresponding electrochemical properties can be controlled by the mixing procedure of starting materials. Figure 9a and b display the SEM and TEM image (SAED pattern) of sample 1 (S1), and the exposed planes were indexed as (010); while the SEM and TEM image (SAED pattern) of sample 2 (S2) (Figure 9c and d) show the main exposed (100) planes. The electrochemical results illustrated that the above two kinds of LFP nanoplates with different crystal orientation demonstrate similar discharge capacities of ~ 160 mAh g^{-1} at low rates of 0.1, 0.5, and 1 C, but quite different ones at high rates (5 and 10 C-rates). The S1 with (010) planes delivered 156 mAh g^{-1} at 5 C-rate and 148 mAh g^{-1} at 10 C-rate, while the S2 with (100) planes delivered only 132 mAh g^{-1} at 5 C-rate and 28 mAh g^{-1} at 10 C-rate, respectively. The results demonstrated that the crystal orientation greatly affect the electrochemical properties of LFP nanoplates, and confirmed that the (010) planes could improve the rate performance. Pei et al.[69] used a hydrothermal reaction to prepare LFP/C nanoparticles, nanoplates and nanorods with controlled *b*-axis thickness by changing the concentration of sodium dodecyl benzene sulfonate (SDBS). The results illustrated that the *b*-axis thickness play a critical role on the percentage of (010) planes and further on the electrochemical performances of the LFP/C nanocomposites. With decreasing the *b*-axis thickness, the LFP/C nanoplates exhibited considerably enhanced electrochemical properties in comparison with those of larger *b*-axis thickness (Figure 9f), owing to the higher percentage of (010) planes for smaller *b*-axis thickness. In the results reported by Saravanan and co-workers, [75] by using a simple solvothermal route, different nanostructures of LFP including hierarchical nanoplates, spindle shape, thick plates and diamond shaped microcrystals were synthesized by just changing the Fe precursor. The electrochemical results indicated that the reversible capacity and rate capability increased also with the decrease in thickness of the nanoplates. Hierarchical LFP/C with thickness of around 30 nm presented the highest reversible capacity of 167 mA h g^{-1} among other LFP/C materials at a current density of 17 mA g^{-1} with a voltage range of 2.3-4.3 V (Figure 9g). Nan et al. [76] reported a uniform LFP nanoplates with high (010) planes exposure also by a solvothermal reaction. They found that the ethylene glycol could act as a surface structure mediator to tune the crystal growth orientation and particle size. Electrochemical results demonstrated that the nanoplates can maintain a reversible capacity of 165 mAh g^{-1} at 0.1 C-rate and 140 mAh g^{-1} at 5 C-rate. In general, LFP nanoplates could be synthesized through various routes, and it is found that the surfactants, precursors, reaction time and temperature greatly affect the resulted status of nanoplates and hence the electrochemical properties of LFP.

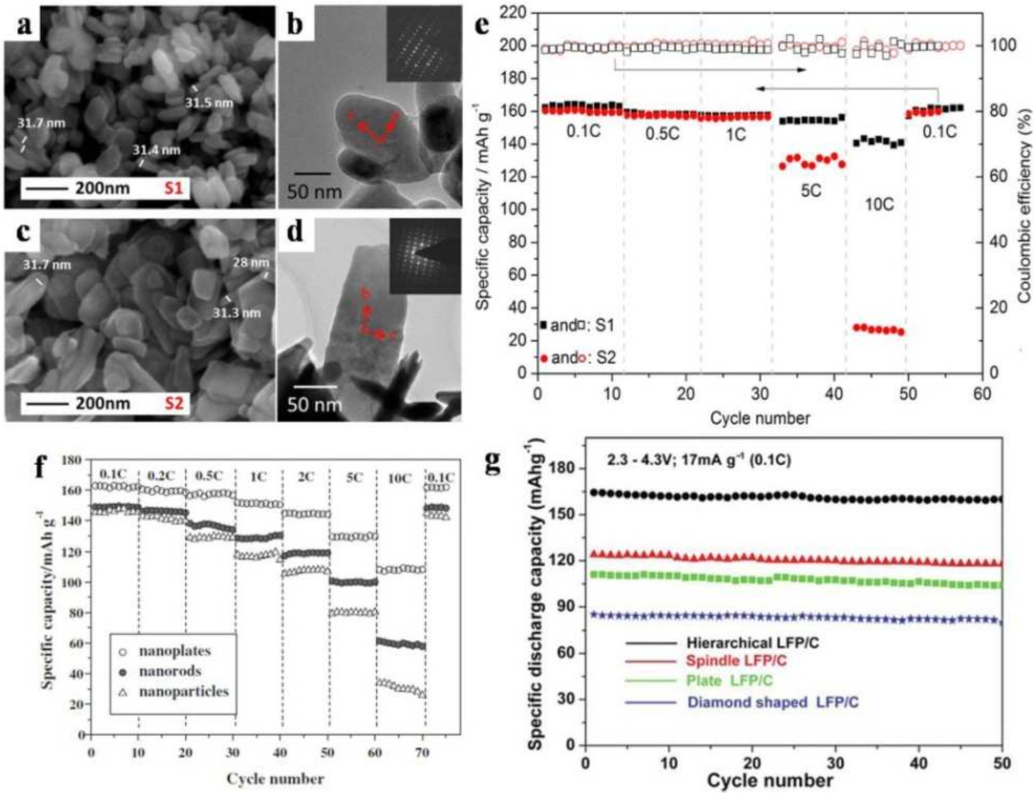

Figure 9 SEM images and TEM images (SEAD inside) of (a, b) S1 and (c, d) S2. (e)

Comparison of the rate performance of S1 and S2.[68] (f) Rate performances of LFP/C nanoparticles, nanorods and nanoplates.[69] (g) Capacity vs. cycle number plots of all LFP/C nanoplates.[75] Reproduced with permission.[68, 69, 75] Copyright 2012 American Chemical Society. Copyright 2012 Elsevier. Copyright 2010 Royal Society of Chemistry.

1D nanostructures of LFP. 1D LFP nanostructures such as nanorods and nanowires with exposed (010) planes have also been studied in the past decades. First of all, it is well known that the 1D nanostructures could accelerate the transportation of lithium ions and electrons during charge/discharge processes, and the exposed (010) planes could further facilitate the transportation of lithium ions as mentioned above. Moreover, carbon coating or incorporation LFP with carbon matrix could further improve their electrochemical performances.

Song et al. [77] reported monodispersed LFP nanocrystals of diverse morphologies via a mild and controllable solvothermal approach with a mixture of ethylene glycol and oleic acid as solvent. They found that the volume ratio of oleic acid to ethylene glycol play a critical role on the resulted morphology of LFP nanoparticles. The SAED patterns and HRTEM images indicated that the dominated crystal planes of all the three LFP samples are (010) planes (Figure 10a). Electrochemical charge/discharge results indicated that the LFP/C nanorods could release a reversible capacity of 155 mA h g^{-1} at 0.5 C-rate and with a capacity retention of 80% at high rate of 5 C-rate, demonstrating a superior rate performance (Figure 10b). Nan and co-workers[78] reported a systematic study that examined the synthesis in ethylene glycol of LFP nanocrystals with six distinct shapes, namely spindle, rod, urchin, small-particle, cuboid and flower-like, demonstrating size and shape control of LFP. It was noteworthy that the size and shape of the as-prepared LFP nanocrystals can be controlled by the ratio and addition sequence of the reagents. The LFP/C nanorods with the predominant (010) planes exposure present the best rate performance among the six distinct LFP particles. Long and co-workers[79] reported an in-situ synthesis of superior high-rate LFP/C nanorods embedded in graphene matrix via hydrothermal synthesis, and the SAED pattern revealed that the rod-like particle is a single crystal with the *b*-axis along the thinnest radical direction, which could favor the transport of Li^+. Besides the preparation of nanorod-like active particles, the use of a graphene matrix and thin carbon coating, which synergically acted as a mixed conductive matrix, enabled fast electronic and ionic transportation.

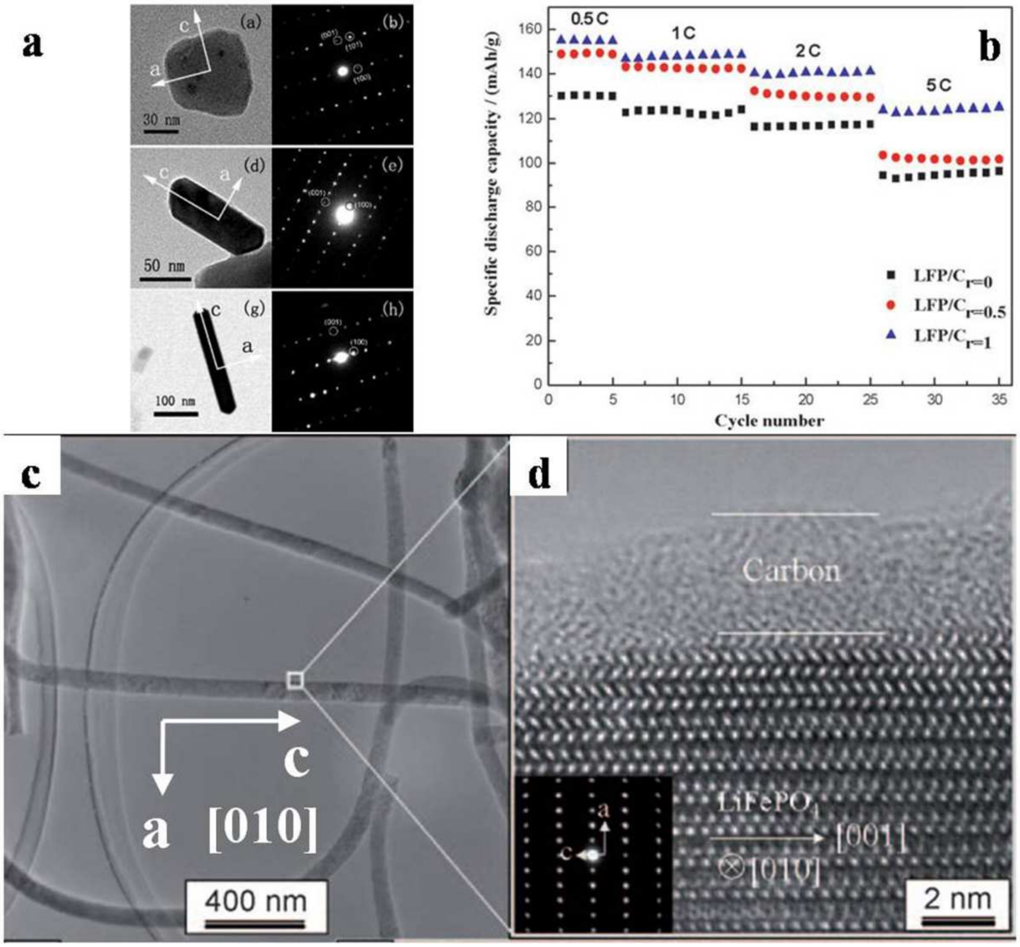

Figure 10 (a) Low-magnification TEM images, selected area electron diffraction (SAED) and high resolution TEM (HRTEM) images and (b) comparison of rate performance of an individual LFPr=0 , LFPr=0.5 and LFPr=1.[77] (c) Overview TEM micrograph showing nanowires with a diameter of around 100 nm. (d) Corresponding high-resolution (HR) TEM image from the marked region, inset: SAED pattern, region of 500 nm in diameter.[64] Reproduced with permission. [77, 85] Copyright 2014 Royal Society of Chemistry. Copyright 2011 Wiley-VCH.

LFP nanowires are also considered as one of the most appealing candidates owing to their unique crystalline texture in comparison with conventional nanoparticles. However, only a few studies about LFP nanowires were reported so far. Lim et al. [80] synthesized LFP nanowires by using a template method, which was rather complicated as it included post-synthesis treatment with HF or NaOH that can dissolve or chemically react with LFP. Wang et al. [81] reported LFP nanowires with diameters in the range of a few hundred nanometers and lengths extending a few tens of micrometers by hydrothermal method, leading to a moderate specific capacity. The electrospinning method is an effective technique to develop 1D nanostructures.[82, 83] Hosono and co-workers[84] prepared triaxial LFP nanowires with a vapor-grown carbon-fiber (VFCF) core-column and a carbon shell by the electrospinning method. However, the thickness of the LFP nanowires (over 500 nm up to 1 μm in diameter, corresponding to a low percentage of (010) planes) significantly constrained their performance. Zhu et al. [685] successfully synthesized carbon-coated single-crystalline LFP nanowires with diameters of 100 nm also by electrospinning method (Figure 10c). The HRTEM image and the SAED pattern (Figure 10d) revealed that the growth direction is along the *c* axis, leading to short transport pathways along the *b* and *a* direction. The unique structure of LFP nanowires demonstrated both high discharge capacities and excellent rate capability, which can deliver a high reversible capacity of 169 mAh g^{-1} at 0.1 C-rate, and still 93 $mAhg^{-1}$ at high rate of 10 C-rate. Future work in this direction may focus on optimizing the electrospinning process to decrease the diameter of LFP nanowires, and therefore increase the percentage of (010) planes to further improve their electrochemical performances.

It is obvious that both theoretical and experimental studies reveal that the (010) planes are highly electrochemical active for LFP cathodes. Solvothermal and hydrothermal reaction are two effective strategies to prepare LFP with increased percentage of (010) planes. The selection of chelating agent, reaction temperature and time, composition and concentration of surfactant significantly affect the growth of LFP nanocrystals, and hence their electrochemical behaviors. The key point is to keep LFP grow along the *ac* plane and decrease the thickness of *b*-axis as much as possible, leading to more (010) planes exposure.

2.3 Spinel cathode materials

2.3.1 $LiMn_2O_4$

Another case of electrochemical facet-dependent properties is spinel cathode materials. Thanks to the inherent low-cost, environmental benign and natural abundance as well as commendable safety, spinel-type lithium manganese oxide ($LiMn_2O_4$) has been regarded as one of the most appealing candidates for cathode materials of the next generation LIBs.[86, 87] However, the rapid capacity fading, which was originated from the dissolution of Mn^{3+} via a disproportionation reaction in electrolytes and the structural degradation during phase transition from cubic to tetragonal structure caused by Jahn-Teller distortion of MnO_6 octahedra, has limited strongly its practical application.[83] Hirayama et al. [88] discussed the resistance of electrode to Mn dissolution on basis of atomic stacking of pristine $LiMn_2O_4$. Figure 11 illustrates the surface structures of $LiMn_2O_4$ (111) and (110) orientations. The (111) planes are terminated by a cubic closely-packed oxygen arrangement in the spinel structure, whereas no closely-packed arrangement of oxygen appear on the (110) planes. The manganese ions are less densely arranged in the (110) planes and are expected to be in close contact with electrolytes. This structure results in that the manganese ions highly reactive with solvents in electrolyte, which as consistent with the (110) planes being less stable than the (111) planes.

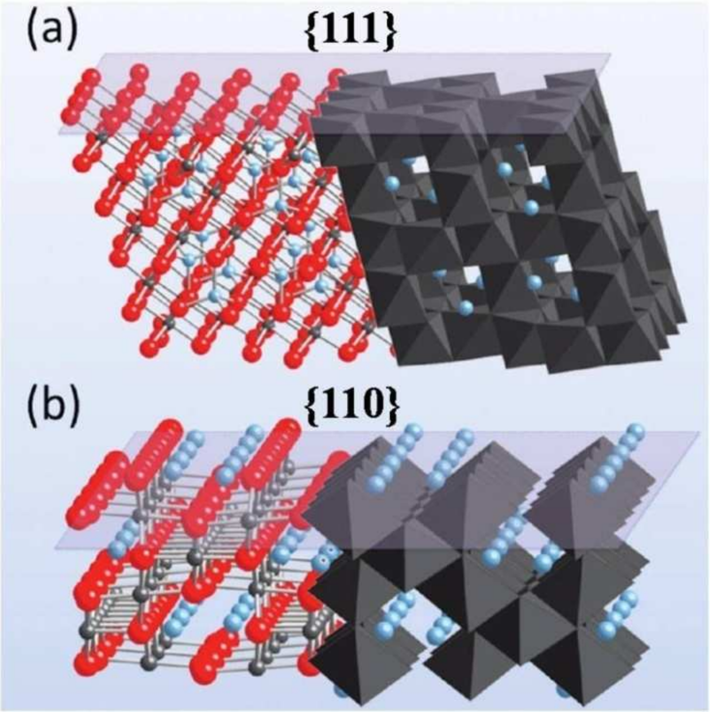

Figure 11 Atomic stackings of $LiMn_2O_4$ (a) (111) and (b) (110) orientations. Reproduced with permission.[88] Copyright 2010 American Chemical Society.

However, it is also obvious to observe that the orientation of (110) planes are aligned to Li diffusion, which can support fast lithium insertion/extraction. Many reported $LiMn_2O_4$ nanostructures enclosed by (110) planes indeed demonstrated excellent electrochemical performance. Cho and co-workers[89] reported that carbon-coated single-crystalline $LiMn_2O_4$ nanoparticle clusters with the diffraction pattern along the $[\bar{1}10]$ zone axis exhibited high specific capacity, long cycleability and high rate capability. $LiMn_2O_4$ nanotubes,[90] nanorods[91, 92] and nanowires[93] with (110) planes exposed were also prepared and shown significantly enhanced rate capability and a high reversible specific capacity. Nevertheless, there were few reports concerning $LiMn_2O_4$ nanostructures enclosed by (111) planes so far. Porous $LiMn_2O_4$ nanosheets composed of single-crystalline $LiMn_2O_4$ nanorods with exposed (111) planes via an in situ lithiation of ultrathin MnO_2 nanosheets were reported by Yuan and co-workers.[94] However, according to the HRTEM image and SAED pattern, the $LiMn_2O_4$ nanorods were actually enclosed by (110) planes rather than (111) planes.

Another interesting concept was developed by Kim et al. [95] A truncated octahedron was prepared through solid state reaction of lithium hydroxide monohydrate with Mn_3O_4 truncated octahedron that was synthesized by hydrothermal reaction. Most surfaces were aligned to the crystal orientations ((111) planes) activating minimal Mn dissolution, while a small portion of surfaces ((110) planes) were truncated along the directions that support Li diffusion (Figure 12a). Octahedral structure enclosed by (111) planes and nanoplates with even smaller dimensions (Figure 12b, c) were also synthesized for comparison. As clearly shown in the surface atomic arrangements of $LiMn_2O_4$ (Figure 12d, e and f), the (110) planes offered fast diffusion channels for lithium ions, while (111) planes were enclosed by a cubic closely-packed oxygen arrangement that resulted a high stability in electrolyte. The electrochemical test results illustrated that the truncated octahedral structure bearing the dual lattice orientations within a single crystal structure exhibit far better performance in both power and cycle life simultaneously (Figure 12g, h and i), resolving the previously conflicting aspects of $LiMn_2O_4$. There are no general agreements about the best proportion of (111) planes and (110) planes, but all the above results disclosed that the electrochemical behaviors of $LiMn_2O_4$ are very sensitive to its surface structures.

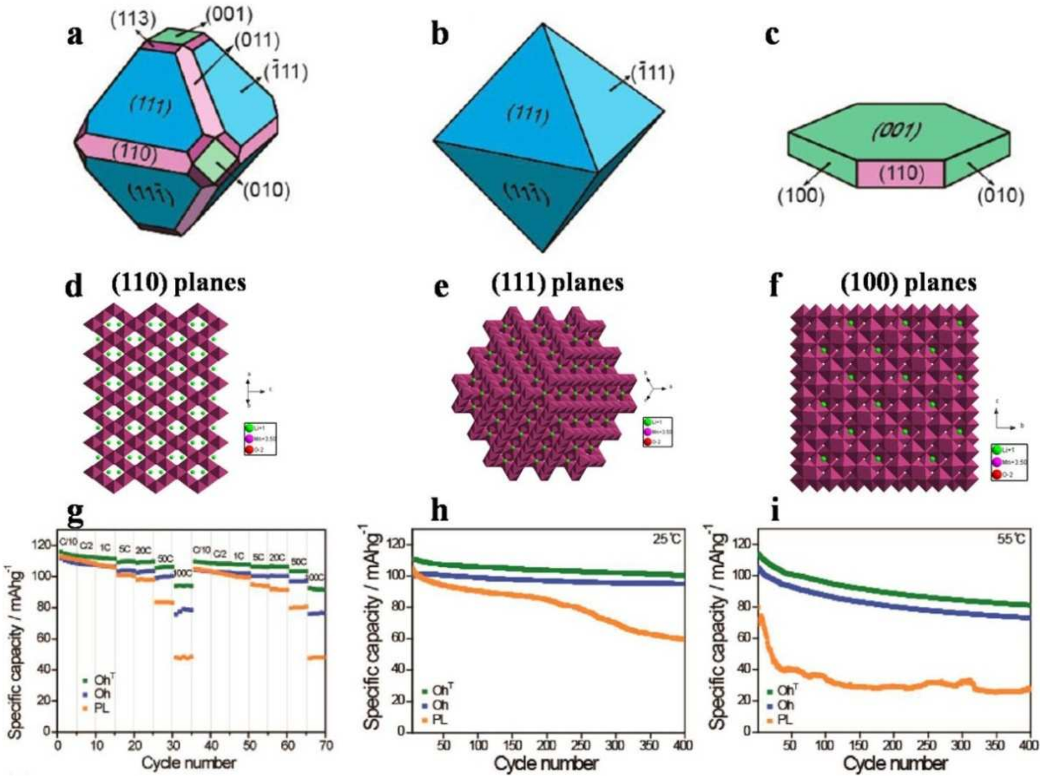

Figure 12 Schematic illustration of $LiMn_2O_4$ with various crystal shapes. (a) Truncated octahedron (OhT). (b) Bare octahedron (Oh). (c) Platelet (PL). The surfaces with equivalent crystal orientations are presented in the same colors. Surface atomic arrangement of different crystal planes of $LiMn_2O_4$: (d) (110) planes, (e) (110) planes and (f) (110) planes. (g) Rate capability tests measured at various C-rates for discharge. Discharge capacities over repeated cycles when cycled at 1 C for charge and 10 C for discharge at (h) 25 and (i) 55 °C.[95] Reproduced with permission.[95] Copyright 2012 ACS Chemical Society.

2.3.2 $LiNi_{0.5}Mn_{1.5}O_4$

Nickel-doped spinel-type cathode material—$LiNi_{0.5}Mn_{1.5}O_4$ has also attracted extensive attention as a result of its higher working voltage range of ~ 4.7 V, in comparison with 4.0 V for $LiMn_2O_4$ spinel cathode (Mn^{3+}/Mn^{4+}).[96-99] The intrinsically fast Li^+ diffusion within the three-dimensional spinel structure leads to a good rate capability, making $LiNi_{0.5}Mn_{1.5}O_4$ attractive for vehicle applications. However, the electrochemical properties of $LiNi_{0.5}Mn_{1.5}O_4$ are very sensitive to the presence of

Mn^{3+}, which may form Mn^{2+} through the disproportion reaction. Mn^{2+} then dissolves into electrolyte, especially at elevated temperatures, leading to significant capacity loss during cycling. From the above analysis about the effect of surface structures on the dissolution of Mn^{3+}, the (111) planes are more stable than the (110) planes. Based on this concept, Manthiram et al. [100] presented a comparison of stoichiometric $LiNi_{0.5}Mn_{1.5}O_4$ cathodes with a 3:1 Mn/Ni ratio prepared by different methods with varying morphologies and degrees of cation ordering. They prepared cubic, truncated, octahedral and spherical samples (Figure 13a), respectively. The electrochemical results indicated that the octahedral material with high (111) planes exposure demonstrated the highest reversible capacity and the best rate capability. In contrast to the results illustrated by Kim and co-workers,[95] the truncated $LiNi_{0.5}Mn_{1.5}O_4$ sample with the presence of (110) planes exhibited poor electrochemical performance. This may be due to that the intrinsically fast Li^+ diffusion of $LiNi_{0.5}Mn_{1.5}O_4$ may reduce the impact of the diffusion channels and emphasize the effect of the dissolution of Mn^{3+}. Another study about the effect of surface facets on the kinetic properties of $LiNi_{0.5}Mn_{1.5}O_4$ cathode materials was reported by Hai and co-workers,[101] in which the structure, kinetic properties, and phase transition mechanism of spinel Li $Ni_{0.5}Mn_{1.5}O_4$ cathode materials were compared on similarly sized (112)-faceted plate crystals and (111)-faceted octahedral crystals. In spite of a more ordered structure, a lower Mn^{3+} content, and significantly larger two-phase regions in the phase diagram, the octahedrons delivered better rate capability and had a much larger chemical diffusion coefficient than did the plates, both of which are attributed to the superior particle morphology of the octahedrons. The results demonstrated that particle morphology has a dominant effect on spinel transport properties.

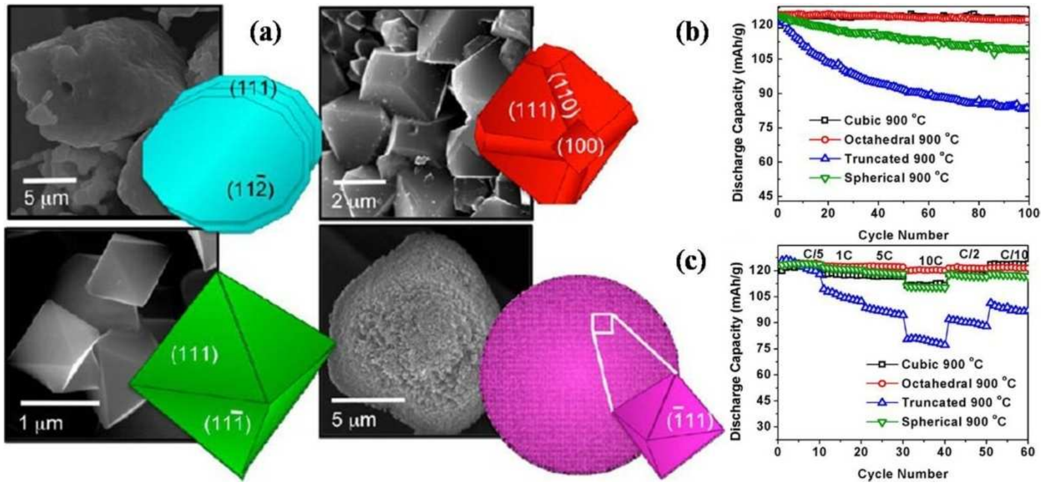

Figure 13 (a) SEM images and schematic surface facets representation of the morphologies of the Cubic, Truncated, Octahedral and Spherical samples prepared at 900 °C. Electrochemical properties of the samples prepared at 900 °C: (b) capacity retention at 0.5 C and (c) rate capability. Reproduced with permission.[100] Copyright 2013 American Chemical Society.

The previous studies proved that the surface orientation has a great influence on the dissolution of Mn^{3+} into electrolyte and diffusion kinetics of lithium ions, resulting in different electrochemical behaviors of spinel cathodes. For $LiMn_2O_4$, the diffusion kinetics of lithium ions makes the (110) planes being the dominated factor; while the dissolution of Mn^{3+} into electrolyte strongly limits the electrochemical performance of $LiNi_{0.5}Mn_{1.5}O_4$, leading to high significance of (111) planes.

3. Nanostructured sulfur cathodes for Li/S batteries

Rechargeable lithium/sulfur (Li/S) batteries have attracted worldwide attention owing to their ultra high specific energy (2600 Wh kg^{-1}) compared to traditional intercalation cathode materials.[102] In a conventional Li/S cell, it is comprised of a lithium metal anode, an organic electrolyte and a sulfur/carbon composite cathode (Figure 14a). Although Li/S batteries have considerable advantages on the energy density and cost, there are still tremendous scientific and technological challenges remained for its practical application. It is well known that Li/S batteries suffer from low utilization of sulfur, poor reaction kinetic and inferior charge/discharge efficiency owing to its poor electronic and ionic conductivity, intrinsic polysulfides (PS) shuttle and Li corrosion (Figure 14b). Therefore, the construction of fast diffusion paths for lithium ions and electrons as well as good trapping of polysulfide shuttle within nanostructured sulfur cathode are the key factors to improve the electrochemical performances.

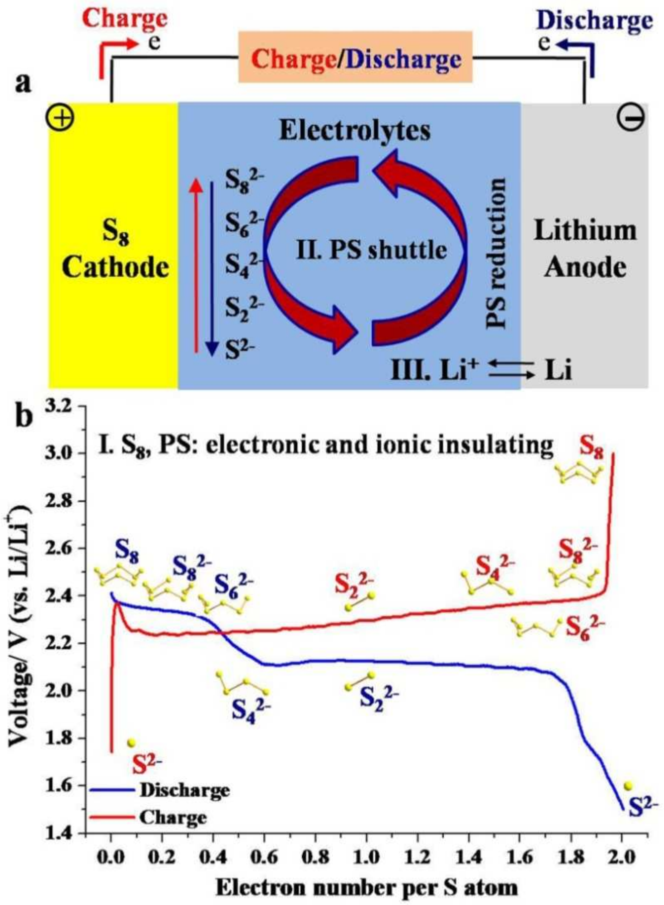

Figure 14 (a) Scheme for the discharge (blue) and charge (red) process involved in a typical Li/S battery. (b) Scheme for discharge (blue) and charge (red) process involving the formation of the lithium polysulfides.

In the past few years, lots of attempts have contributed to construction of nanostructured sulfur cathodes, in which sulfur nanoparticles are well incorporated with various carbonaceous materials through physical adsorption, chemical bonding and surface modification.[103] Some developments of Li/S batteries have been summarized recently and important comments on the main challenges for large scale application of Li/S batteries are also outlined.[5, 104-122] Generally, the ideal carbonaceous material for sulfur/carbon composites should possess the following merits: (1) high electronic conductivity for efficient electron transport to achieve a high specific capacity and a high rate capability; (2) good affinity for sulfur active materials through chemical and physical means to accommodate the polysulfide shuttle phenomenon; (3) good accessibility of liquid electrolyte to active material; (4) stable framework to sustain the strain generated by the volume changes of active material during cycling. Among them, graphene-based carbonaceous materials and micro-mesoporous carbon materials have been extensively studied. Owing to different properties of carbonaceous materials, the electrochemical performances of sulfur/carbon composites are quite different. In this section, we will focus on the synthesis of sulfur/carbon composites for Li/S batteries, and discuss the design principle, structure and properties of these nanostructured sulfur cathodes in the order of 2D graphene-based carbon materials, 3D micro-mesoporous carbon materials and hierarchical carbon materials.

3.1 2D graphene-based carbon materials

The poor electronic conductivity of sulfur (5×10^{-30} S cm^{-1} at 25 °C) and polysulfides decreased largely the utilization of sulfur active materials in cathodes owing to very low electron transportation kinetic.[123] 2D carbon-graphene-based carbon materials draw intensive attention in the study of Li/S batteries due to their ultra high electronic conductivity. Diverse structures of sulfur/graphene composites such as graphene-wrapped sulfur particles,[124-128] sandwich structure[129-131] and sulfur-coated graphene composite[132, 133] were developed through different synthetic routes. The key point is to increase the reaction kinetics of polysulfides and simultaneously retain them at the cathode. In 2008, Wang et al. firstly reported a sulfur/graphene composite by heating a mixture of graphene nanosheets and elemental sulfur, in which the highly porous graphene nanosheets were prepared by a solvothermal method.[134] The charge/discharge results indicated that the sulfur/graphene composite greatly increased the electrical conductivity, reversible capacity and cycle stability compared to the bare sulfur electrode. However, the sulfur content was only 22 wt.%, resulting to a low energy density of S/graphene composite. A systematic study between the sulfur loading and the corresponding electrochemical properties of S/expanded graphite (S/EG) composites that were prepared by a melt-diffusion strategy was done by Wang et al,[135] in which expanded graphite was composed of loosely stacked graphene sheets with a preserved layered structure. The elemental mapping images of S/EG-0.6 (Figure 15a) revealed that sulfur is homogeneously embedded into the framework of the graphene host. The electrochemical results demonstrated that the nanocomposite with 60 wt.% sulfur content exhibited the highest capacity. It demonstrated an initial discharge capacity of 1210.4 mAh g^{-1} and retained as high as 879.5 mAh g^{-1} at a charge/discharge current density of 280 mA g^{-1} after 70 cycles. Moreover, an improved cycleability, a dwindled over-charged phenomenon and an outstanding rate capability were also confirmed.

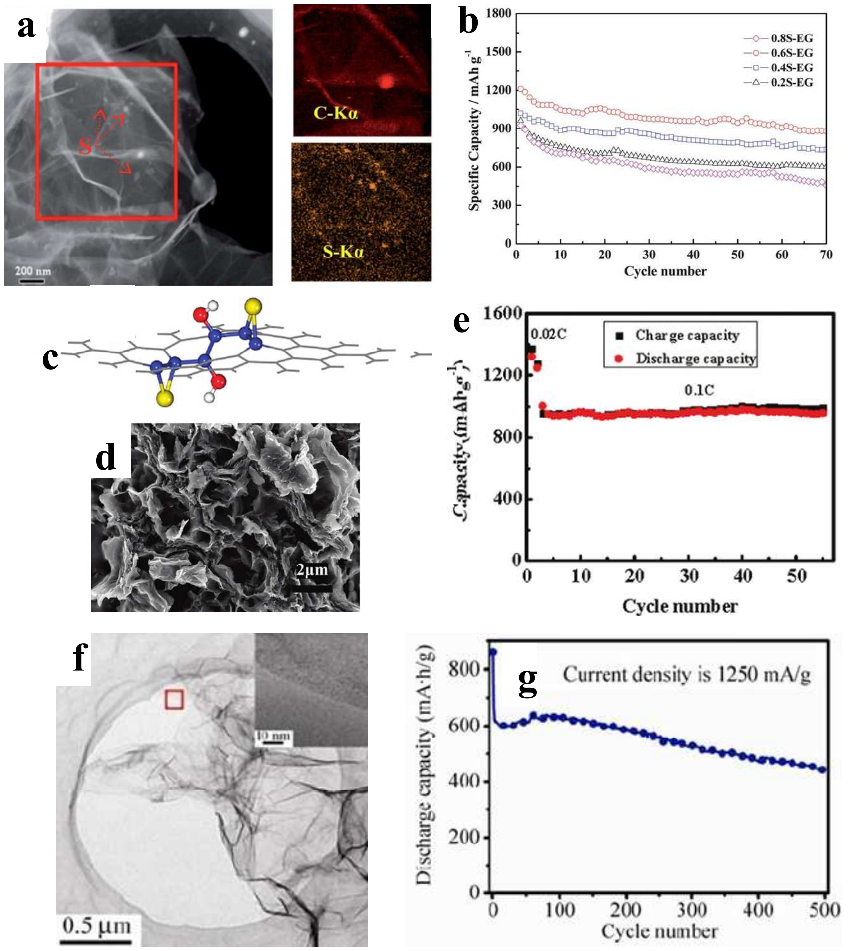

Figure 15 (a) Elemental mappings of carbon and sulfur of the 0.6S/EG nanocomposite. (b) Cycle performances of S/EG composites with different sulfur loading.[135] (c) Representative pattern of GO immobilizing S. (d) SEM image of the GO-S nanocomposite. (e) Cycling performance of GO/S nanocomposite at a constant current rate of 0.1 C after initial activation processes at 0.02 C for two cycles.[136] (f) TEM image of SGC-63.6%S. (g) Cycling performance of SGC-63.6%S at 1250 mA g^{-1} (0.75 C).[137] Reproduced with permission.[135-137] Copyright 2012 Royal Society of Chemistry. Copyright 2011 American Chemical Society. Copyright 2012 Springer.

Ji and co-workers[138] reported a chemical approach to immobilize sulfur and lithium polysulfides via the reactive functional groups on graphene oxide, which can obtain a uniform and thin (around tens of nanometers) sulfur coating on graphene oxide sheets with 66 wt.% sulfur content by a wet chemical reaction process (Figure 15c and d). The GO/S composite could maintain a reversible capacity of 954 mAh g^{-1} with a coulombic efficiency of 96.7% after 50 cycles, demonstrating a good cycleability and improved coulombic efficiencies (Figure 15e). Such excellent properties should be benefited from the strong interaction between graphene oxide and sulfur or polysulfides as confirmed by *ab* initio calculations and X-ray absorption spectroscopy. A graphene oxide/wrapped sulfur composite also synthesized through wet-chemical reaction process by Wang and co-workers, and exhibited improved cycleability and rate capability.[125] As the GO could be reduced by sulfur-containing compounds such as Na_2S and Na_2SO_3, Sun and co-workers[137] further reported a sulfur/reduced graphene oxide composite (SGC) materials with uniformly dispersed sulfur on reduced graphene oxide sheets by a simple aqueous one-pot synthesis method, in which the formation of the composite was achieved through simultaneous oxidation of sulfide and reduction of graphene oxide. XPS, FTIR and XRD results confirmed that the majority of GO was reduced during the synthesis process, and the electrical conductivity of the sulfur/reduced graphene oxide composite (1.30 S cm^{-1}) was greatly improved compared to that of GO (0.0178 S cm^{-1}). The TEM image (Figure 15f) of SGC-63.6% revealed a uniform distribution of carbon and sulfur in the composite. As a result, the SGC-63.6%S presented an impressive long cycling stability of a reversible capacity of 440 mAh g^{-1} after 500 cycles of charge/discharge at high current density of 1250 mA g^{-1} (Figure 15g). Recently, Zhou and co-workers[139] designed a unique sandwich structure with pure sulfur between two graphene membranes, in which one membrane was used as a current collector with sulfur coated on it as active material, and the other graphene membrane was coated on a commercial polymer separator. The sulfur powder electrode with two graphene membranes can provide rapid ion and electron transport paths, accommodate sulfur volumetric expansion, store and reuse migrating polysulfides to alleviate the shuttling effect. It can deliver a reversible capacity of 680 mAh g^{-1} with a coulombic efficiency above 97% at 1.5 A g^{-1} after 300 cycles. In summary, graphene-based carbonaceous materials significantly improved the electrochemical performances of sulfur cathodes in Li/S batteries.[138-142] It is expected that the previous and under-going researches will promote the commercial application of Li/S batteries in the near future.

3.2 3D porous carbon materials

3D microporous carbon composites. Owing to the tiny size of S_8 molecule (0.088 nm), microporous carbon materials (<2 nm) was employed as carbon host in Li/S batteries, which is expected to commendably trap polysulfides species, therefore decrease the loss of sulfur active materials and inhibit polysulfide shuttle. Zhang and co-workers[143] reported a sulfur/carbon sphere composite by encapsulating sulfur into micropores of carbon spheres through thermal treatment of a mixture of sublimed sulfur and carbon spheres. The sulfur/carbon sphere composite with 42wt.% sulfur presented a long electrochemical stability up to 500 cycles, based on the constrained electrochemical reaction inside the narrow micropores of carbon spheres due to strong adsorption. However, after increasing the sulfur content to 51wt.%, the reversible capacity of sulfur/carbon sphere composite decreased quickly to 300 mAh g^{-1} even at a low current density of 40 mA g^{-1}, ascribing to the pore narrowing and full saturation of the micropores. Metal-organic framework (MOF) derived microporous carbon has recently attracted attention in Li/S batteries.[144, 145] However, they presented also moderate electrochemical performance with high sulfur loading. Recently, Wu and co-workers[145] embedded sulfur in metal-organic framework-derived microporous carbon polyhedrons (MPCP), and the electrochemical results illustrated that the sulfur/MPCP composite with a sulfur loading of 43wt.% decay to 420 mAh g^{-1} after 100 cycles at 100 mA g^{-1} in DOL/DME electrolyte. Therefore, it is a great challenge to synthesize high performance sulfur/microporous carbon composites with high sulfur loading.

3D mesoporous carbon composites. Mesoporous carbon materials (2-50 nm) possess uniform pore size, high specific surface areas, high pore volumes and interconnected porous structures, and can possess high electronic conductivity, which has a wide application in the study of lithium ion batteries.[146, 147] The mesoporous carbon can serve as a good matrix to trap the dissolved polysulfides and increase the electronic conductivity of sulfur/mesoporous carbon composites in Li/S batteries. Nazar and co-workers reported a nanoporous sulfur cathode based on a mesoporous carbon (CMK-3) (Figure 16a).[148] The conductive CMK-3 framework precisely constrained sulfur nanofiller within its channels, and generated essential electrical contact to the insulating sulfur as well as access to Li^+ ingress/egress for reactivity with the sulfur, resulting in a high initial discharge capacity of 1020 mAh g^{-1} for S/CMK-3 composite with 70wt.% sulfur loading. It can be further improved by a polymer coating, which can help retard diffusion of polysulfides out of the cathode structure, minimizing thus the loss of active mass in the cathode and improve the cycling stability (Figure 16b).

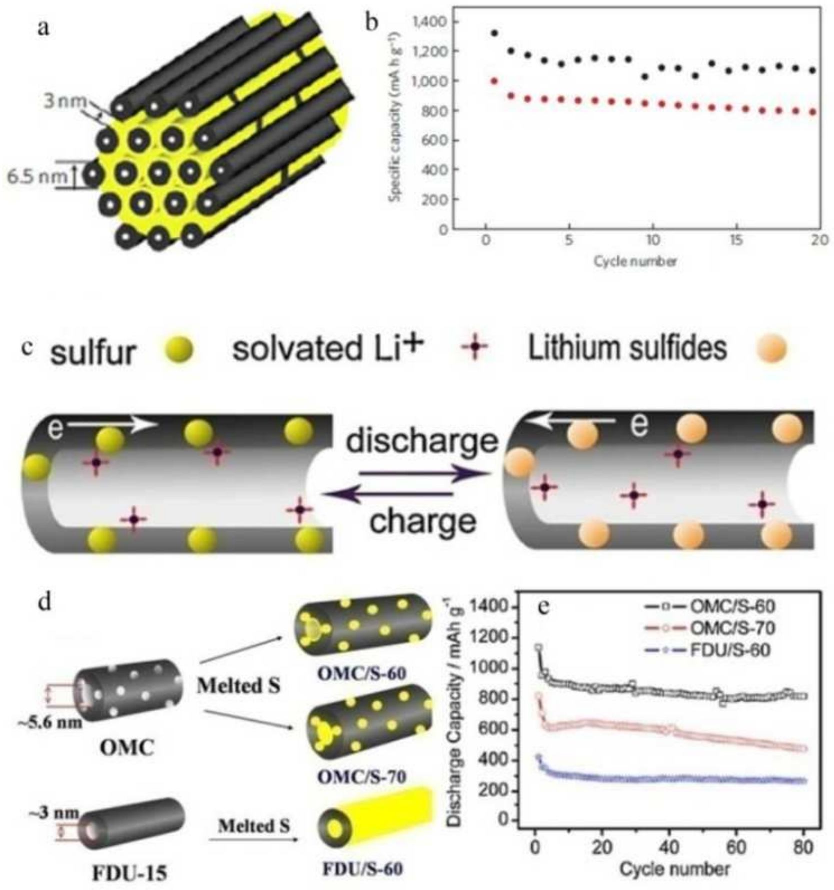

Figure 16 (a) A schematic diagram of sulfur (yellow) confined within the interconnected pore structure of CMK-3. (b) Cycling performance of CMK-3/S modified with PEG (upper points, in black) versus CMK-3/S (lower points, in red) at

168 mA g^{-1} at room temperature.[148] (c) Schematic illustration of the discharge–charge process and transport paths of both lithium ions and electrons in the OMC/S-60 nanocomposite cathode; (d) Schematic diagrams of the optimized loading of sulfur in OMC and FDU-15 carbon; (e) Cycling curves of the OMC/S-60, OMC/S-70, and comparative FDU/S-60 nanocomposite cathode at a 0.1 C rate.[149] Reproduced with permission.[148, 149] Copyright 2009 Nature publishing group. Copyright 2010 Elsevier.

Chen et al.[149] reported another ordered mesoporous carbon/sulfur (OMC/S) composite by a simple melt-diffusion method, in which the OMC has a bimodal meso/microporous structure (2.3 nm and 5.6 nm) and a high surface area (2102 m^2 g^{-1}) as well as a high pore volume (2.0 cm^3 g^{-1}). The small mesopores could serve as “nano-reactor” for sulfur nanoparticles, while the big mesopores could provide a short diffusion path for lithium ions and electrolytes, and the kinetic of electron conduction was greatly increased at the large interfacial contact area between sulfur nanoparticles and OMC through the OMC framework (Figure 16c). The electrochemical results demonstrated that the OMC/S-60 exhibit a very stable reversible capacity as high as 800 mAh g^{-1} within 80 cycles at a charge/discharge rate of 0.1 C-rate (Figure 16e), and a reversible capacity of 415 mAh g^{-1} after 400 cycles at a high rate of 2.7 C-rate. In the case of OMC/S-70 and FDU/S-60, part of their mesopores were blocked by sulfur nanoparticles owing to excess sulfur loading, they presented much lower specific capacities than OMC/S-60 at the same rate (Figure 16b and c). The results disclosed that the diffusion path for lithium ions and electrons during charge/discharge process strongly affect the electrochemical behaviors of sulfur cathodes. Nazar and co-workers[150] also reported spherical ordered mesoporous carbon nanoparticles with a bimodal pore size distribution and the highest inner pore volume of 2.33 cm^3 g^{-1} as well as the highest surface area of 2445 m^2 g^{-1}. The C/S spherical electrodes showed a high reversible charge capacity of up to 1200 mAhg^{-1} and good cycling stability. The performance of the cells could be further improved by either removing the external sulfur on the surface or by adding a thin coating of SiO_x. However, another work about mesoporous carbon composite with bimodal pore size in Li/S batteries reported by Liang and co-workers[151] exhibited inferior electrochemical performance than the results reported by Chen et al.[149] and that of Nazar et al.[150], indicating a great influence of the inherent mesoporous carbon structures. They employed KOH activation on pre-prepared mesoporous carbon materials to create a bimodal meso/microporous carbon. However, in order to maintain a considerable capacity and cycle stability, the sulfur loading was limited to only 11.7 wt.%. Higher sulfur loading will lead to a dramatic capacity fading and low specific capacities. A systematic investigation on the correlations between mesoporous carbon pore structure, sulfur loading, surface modification, and battery performance was studied by Liu and co-workers.[152] A series of mesoporous carbon materials with tunable pore sizes (22 nm, 12 nm, 7 nm, and 3 nm) and pore volumes (up to 4.8 cm^3 g^{-1}) were synthesized using a hard-template approach. They elucidated how the pore structure, sulfur loading, and surface modifications affect the electron and mass transfer in electrochemical reactions, which in turn affected the performance of Li/S batteries.

3.3 Sulfur/hierarchical carbon composites. The electronic conductivity of micro-mesoporous carbon materials was usually lower than other graphite–based materials due to their disordered amorphous nature. As a consequence, studies about hybrid carbon nanostructures were increasing, in which micro-mesoporous carbon was incorporated with other highly conductive carbon materials including graphene, carbon nanotubes and conductive polymers. Xin and co-workers[153] reported multi-walled carbon nanotubes (CNT) with a microporous carbon coating layer via a solution-based method. Metastable small sulfur molecules of S_{2-4} were synthesized in the confined space of a conductive microporous carbon matrix, which can avoid the transition from S_8 to S_4^{2-} during the initial Li uptake process and thereby prevent the formation of polysulfides (Li_2S_n, n=4−8) upon discharging. The as-obtained S_{2-4} in S/(CNT@MPC) showed a high specific capacity of 1670 mAh g^{-1}, an impressive cycling stability of 1149 mAh g^{-1} after 200 cycles, and a favorable high-rate capability of 800 mAh g^{-1} at 5 C-rate. Wang et al.[154] also reported a hierarchical architecture

MWCNT@meso-C core-shell composite by a sol-gel coating method followed by nanocasting, which can exhibit an initial discharge capacity of 1248 mAh g^{-1} although it decayed to about 640 mAh g^{-1} after 50 cycles. Other hybrid carbon structures such as MPC/graphene,[155, 156] MPC/GO[157], MPC/carbon nanotubes,[158] MPC/Polypyrrole[159] and MPC/PANI[160] in Li/S batteries were also reported.

3.4 Progress of sulfur/carbon composites with high sulfur loading

Another challenging issue of Li/S batteries was the sulfur loading in the sulfur/carbon composites, which could increase the gravimetric/volumetric energy densities of Li/S batteries. However, as a result of the electronic insulating nature of elemental sulfur, sulfur/carbon composites with sulfur content over 80 wt.% usually presented rapid capacity fading and low specific capacity.[135, 137, 149] Nazar and Evers[124] prepared a graphene/sulfur composite with 87 wt.% sulfur loading by a simple one-pot and scalable method, in which the graphene enveloped the sulfur particles, providing a conductive shrink-wrap for electron transport (Figure 17a). The obtained GSC could deliver an initial discharge capacity of 705 mAh g^{-1} at 0.2 C-rate, and maintain a reversible capacity of around 500 mAh g^{-1} after 50 cycles (Figure 17b). A peapod-like carbon material with interconnected pore channels and large pore volume of 4.69 cm^3 g^{-1} was also used to prepared sulfur/peapod-like carbon composite with 84 wt.% sulfur loading.[161] Even accounted for only 56 vol.% of the peapod-like carbon, the as-prepared S/C composite could only deliver a capacity of ~ 400 mAh $g^{-1}{}_{(S)}$ after 50 cycles at 0.2 C-rate. The above two results suggesting that the electronic conductivity may be the crucial factor on electrochemical performance of S/C composite with high sulfur loading rather than the pore volume. Another work about sulfur/porous graphitic carbon composites was reported by Xu et al.,[162] in which the porous graphitic carbon was synthesized using sucrose as carbon precursor and $CaCO_3$ as hard template and followed by 1200 °C calcination (Figure 17c). The electrochemical result demonstrated that the obtained composite with a sulfur loading of 88.9 wt.% could maintain an overall discharge capacity of 649.4 mAh $g^{-1}{}_{(comp)}$, capacity retention of 84.6% and a coulombic efficiency of 97.4% after 50 cycles at 0.1 C-rate (Figure 17d). Graphene,[163] 3-D nitrogen-doped graphene,[164] reduced graphene oxide[165] and aligned carbon nanotubes[166] showed significantly improved electrochemical performances for S/C composites with high sulfur loading. It is expected other highly conductive carbonaceous materials with good affinity for sulfur could probably lead to high specific capacities combined with good cycle stability.

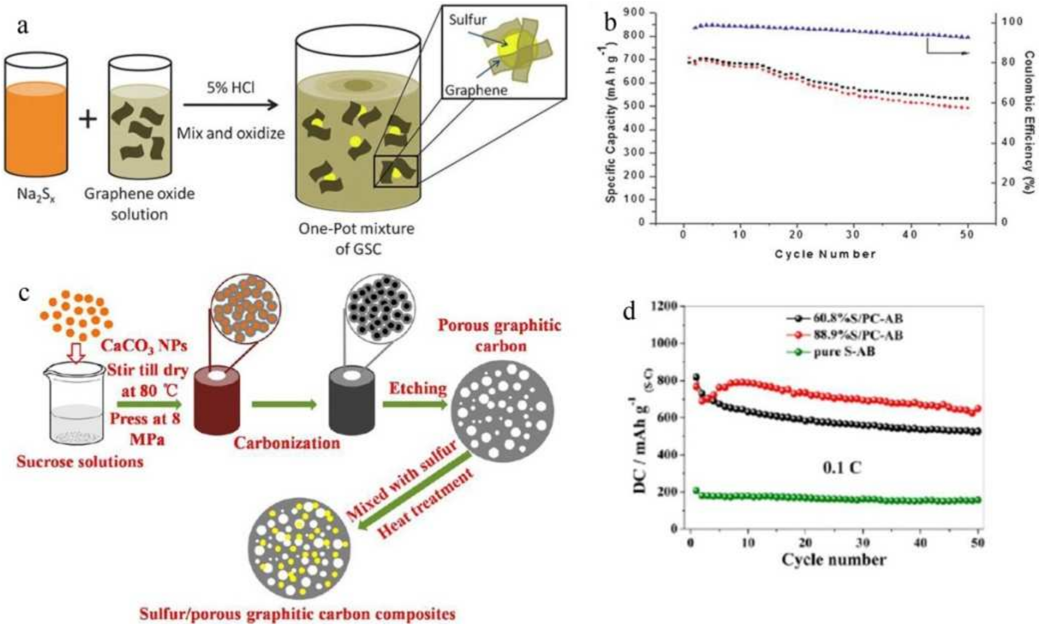

Figure 17 (a) The one-pot synthesis step for the production of GSC with a sulfur loading of 87 wt.%, (b) cycling stability of GSC at 0.2 C with discharge (red), charge (black) and coulombic efficiency (blue).[124] (c) Synthesis route for porous graphitic carbon and sulfur/porous graphitic carbon composite, (d) overall discharge capacities of S-AB, 60.8%S/PC-AB and 88.9%S/PC-AB electrodes verse cycle number at 0.1 C.[162] Reproduced with permission.[124, 162] Copyright 2012 Royal Society of Chemistry. Copyright 2013 American Chemical Society.

4. Summary and outlooks

This review has summarized recent advances on tuning the structure and electrochemical properties of nanostructured cathode materials for lithium ion and lithium sulfur batteries, including layered lithium metal oxide, $LiFePO_4$ and spinel materials as well as sulfur cathodes. The electrochemical properties of electrode materials depend strongly on the transportation kinetics of lithium ions and electrons within the electrodes during electrochemical process. Therefore, construction of electrode materials with fast lithium ions and electrons diffusion paths has attracted intensive attention in the past decades.

Surface structure tuning is one of the best approaches to facilitate the transportation of lithium ions as this process might be crystal facet-sensitive. The relationship between the crystal facets and their electrochemical activities for layered lithium metal oxide, $LiFePO_4$ and spinel cathodes have been analyzed and discussed in detail. This review demonstrates that there are significant challenges toward the rational design and synthesis of battery materials with high percentage of open surface structures owing to their high surface energy, which could dramatically improve their rate property. It is still very difficult to construct high quality battery materials with high percentage of open surface structure that satisfies the requirement of industrial use, such as non-agglomerated state, high tap density, low-cost and large-scale synthesis. Some prospective research directions can be predicted as follows:

(1) The growth mechanism of open surface structure is a key and to be further investigated to provide guidelines for the controlled synthesis of battery materials with open surface structure.

(2) A crucial issue is associated with the stability of open surface structures during long-term charge/discharge processes. The open surface structure may lead to decrease thermal stability owing to their high surface energy, which may induce severe electrolytes decomposition. The surface coating may be therefore an effective way to stabilize the materials.

(3) In-situ high energy X-ray diffraction and in-situ SEM and TEM techniques are strongly recommended to investigate the mechanism and structural evaluation.

(4) First principles and density functional theory (DFT) calculation studies would help understanding the relationship between different surface structures and their electrochemical properties.

On the other hand, the construction of nanostructured sulfur cathodes with fast diffusion paths for lithium ions and electrons as well as good trapping of polysulfide shuttle have drawn intensive attention in the past decades. This review has summarized the research of graphene-based and micro-mesoporous carbon materials for Li/S batteries. The influence of pore structure and electronic conductivity of carbon materials, sulfur loading and morphologies of sulfur/carbon composites on their electrochemical performance are discussed and analyzed. With a rational design of sulfur/carbon nanocomposite and an optimizing sulfur loading, a reversible capacity of 800 mAh g^{-1} with good capacity retention and coulombic efficiencies over 100 cycles at moderate rates have been achieved in many reported studies. However, a series of scientific challenges and technological issues should be overcome before this promising battery system could be commercialized.

(1) It is still a great challenge to synthesize high quality carbon host with high pore volume and high electronic conductivity for ultrahigh sulfur loading, which could approach the high energy of lithium sulfur batteries.

(2) Corrosion of Li anode and formation of lithium dendrite has been considered as a common puzzle in lithium sulfur batteries, as well as in lithium ion batteries and lithium air batteries. A protected lithium anode is required for long-term working lithium sulfur batteries.

(3) The general used electrolyte for lithium sulfur batteries is ether-based electrolytes, which have high dissolubility of polysulfides, leading to loss of sulfur active materials and severe polysulfides shuttle. Other electrolytes such as solid and gel electrolyte could suppress polysulfides dissolution but present low ionic conductivity. Future work may focus on the study of electrolytes with both high ionic conductivity and low dissolution of polysulfides and without decreasing the reaction reversibility.

(4) Smart cell design such as binder-free electrode, separator modification, functional interlayer insertion between separator and cathode side may attract more attention.

(5) The great achievement that has been accomplished in lithium sulfur batteries could promote the development of room temperature sodium sulfur batteries.

In conclusion, structure tuning is an efficient strategy to control the electrochemical performances of electrode materials, and can be extended to other fields such as electro-catalysis, photo-catalysis, gas sensors and super-capacitors.

Acknowledgements

This work is supported by NSFC (21273184, 21373008 and 21321062), and SRFDP (20130121110002).

Notes and Reference

1. J. M. Tarascon and M. Armand, *Nature*, 2001, **414**, 359-367.
2. M. Armand and J. M. Tarascon, *Nature*, 2008, **451**, 652-657.
3. M. R. Palacin, *Chem. Soc. Rev.*, 2009, 38, 2565-2575.
4. R. Marom, S. F. Amalraj, N. Leifer, D. Jacob and D. Aurbach, *J. Mater. Chem.*, 2011, **21**, 9938-9954.
5. P. G. Bruce, S. A. Freunberger, L. J. Hardwick and J. M. Tarascon, *Nat. Mater.*, 2012, **11**, 19-29.
6. D. Marmorstein, T. H. Yu, K. A. Striebel, F. R. McLarnon, J. Hou and E. J. Cairns, *J. Power Sources*, 2000, **89**, 219-226.
7. P. G. Bruce, B. Scrosati and J.M. Tarascon, *Angew. Chem., Int. Ed.*, 2008, **47**, 2930-2946.
8. Y. Yang, M. T. McDowell, A. Jackson, J. J. Cha, S. S. Hong and Y. Cui, *Nano Lett.*, 2010, **10**, 1486-1491.
9. Y. K. Sun, C. S. Yoon, S. T. Myung, I. Belharouak and K. Amine, *J. Electrochem. Soc.*, 2009, **156**, A1005-A1010.
10. M. S. Whittingham, *Chem. Rev.*, 2004, **104**, 4271-4301.
11. Z. Y. Bi, X. D. Zhang, W. He, D. D. Min and W. S. Zhang, *Rsc Adv.*, 2013, **3**, 19744-19751.
12. D. Liu, W. Zhu, J. Trottier, C. Gagnon, F. Barray, A. Guerfi, A. Mauger, H. Groult, C. M. Julien, J. B. Goodenough and K. Zaghi, *Rsc Adv.*, 2014, **4**, 154-167.
13. Z. H. Chen, Y. Qin, K. Amine and Y. K. Sun, *J. Mater. Chem.*, 2010, **20**, 7606-7612.
14. K. T. Lee and J. Cho, *Nano Today*, 2011, **6**, 28-41.
15. A. S. Arico, P. Bruce, B. Scrosati, J. M. Tarascon and W. Van Schalkwijk, *Nat. Mater.*, 2005, **4**, 366-377.
16. Z. Y. Zhou, N. Tian, J. T. Li, I. Broadwell and S. G. Sun, *Chem. Soc. Rev.*, 2011, **40**, 4167-4185.
17. G. Z. Wei, X. Lu, F. S. Ke, L. Huang, J. T. Li, Z. X. Wang, Z. Y. Zhou and S. G. Sun, *Adv. Mater.*, 2010, **22**, 4364-4367.
18. J. J. Wang and X. L. Sun, *Energy Environ. Sci.*, 2012, **5**, 5163-5185.
19. G. L. Xu, J. T. Li, L. Huang, W. F. Lin and S. G. Sun, *Nano Energy*, 2013, **2**, 394-402.
20. X. Xiao, X. Liu, H. Zhao, D. Chen, F. Liu, J. Xiang, Z. Hu and Y. Li, *Adv. Mater.*, 2012, **24**, 5762-5766.
21. Y. Y. Li, Y. X. Jiang, M. H. Chen, H. G. Liao, R. Huang, Z. Y. Zhou, N. Tian, S. P. Chen and S. G.

Sun, *Chem. Commun.*, 2012, **48**, 9531-9533.

22. N. Tian, Z. Y. Zhou, S. G. Sun, Y. Ding and Z. L. Wang, *Science*, 2007, **316**, 732-735.

23. R. S. Devan, R. A. Patil, J. H. Lin and Y. R. Ma, *Adv. Funct. Mater.*, 2012, **22**, 3326-3370.

24. J. Chen, L. N. Xu, W. Y. Li and X. L. Gou, *Adv. Mater.*, 2005, **17**, 582-586.

25. H. J. Yu and H. S. Zhou, *J. Phys. Chem. Lett.*, 2013, **4**, 1268-1280.

26. F. Fu, G. L. Xu, Q. Wang, Y. P. Deng, X. Li, J. T. Li, L. Huang and S. G. Sun, *J. Mater. Chem. A*, 2013, **1**, 3860-3864.

27. J. H. Liu and X. W. Liu, *Adv. Mater.,* 2012, **24**, 4097-4111.

28. J. Liu, J. S. Chen, X. Wei, X. W. Lou and X.-W. Liu, *Adv. Mater.*, 2011, **23**, 998-1002.

29. C. Wang, Y. Zhou, M. Ge, X. Xu, Z. Zhang and J. Z. Jiang, *J. Am. Chem. Soc.*, 2010, **132**, 46-47.30. J. Li, R. Yao and C. Cao, *ACS Appl. Mater. Interfaces*, 2014, **6**, 5075-5082.

31. T. Wei, R. Zeng, Y. Sun, Y. Huang and K. Huang, *Chem. Commun.*, 2014, **50**, 1962-1964.

32. H. Q. Liu, Y. M. Hu, Y. Li and H. S. Gu, *Mater. Chem. Phys.*, 2013, **138**, 440-443.

33. X. L. Xiao, X. F. Liu, L. Wang, H. Zhao, Z. B. Hu, X. M. He and Y. D. Li, *Nano Res.*, 2012, **5**, 395-401.

34. J. Yang, F. Cheng, X. Zhang, H. Gao, Z. Tao and J. Chen, *J. Mater. Chem. A.*, 2014, **2**, 1636-1640.

35. X. Zhang, F. Cheng, J. Yang and J. Chen, *Nano Lett.*, 2013, **13**, 2822-2825.

36. R. S. Devan, R. A. Patil, J. H. Lin and Y. R. Ma, *Adv. Funct. Mater.*, 2012, **22**, 3326-3370.

37. J. M. Li, W. Wan, H. H. Zhou, J. J. Li and D. S. Xu, *Chem. Commun.*, 2011, **47**, 3439-3441.

38. T. Song, J. L. Xia, J. H. Lee, D. H. Lee, M. S. Kwon, J. M. Choi, J. Wu, S. K. Doo, H. Chang, W. Il Park, D. S. Zang, H. Kim, Y. G. Huang, K. C. Hwang, J. A. Rogers and U. Paik, *Nano Lett.*, 2010, **10**, 1710-1716.

39. H. W. Lee, P. Muralidharan, R. Ruffo, C. M. Mari, Y. Cui and K. Kim do, Nano Lett., 2010, **10**, 3852-3856.

40. A. L. M. Reddy, M. M. Shaijumon, S. R. Gowda and P. M. Ajayan, Nano Lett., 2009, **9**, 1002-1006.

41. C. K. Chan, H. L. Peng, G. Liu, K. McIlwrath, X. F. Zhang, R. A. Huggins and Y. Cui, *Nature Nanotech.*, 2008, **3**, 31-35.

42. K. T. Nam, D. W. Kim, P. J. Yoo, C. Y. Chiang, N. Meethong, P. T. Hammond, Y. M. Chiang and A. M. Belcher, *Science*, 2006, **312**, 885-888.

43. D. Luo, G. Li, C. Fu, J. Zheng, J. Fan, Q. Li and L. Li, *Adv. Energy Mater.*, 2014, 4, 1400062.

44. M. G. Kim, M. Jo, Y. S. Hong and J. Cho, *Chem. Commun.*, 2009, **2**, 218-220.

45. X. L. Xiao, L. M. Yang, H. Zhao, Z. B. Hu and Y. D. Li, *Nano Res.*, 2012, **5**, 27-32.

46. F. Cheng, Y. Xin, J. Chen, L. Lu, X. Zhang and H. Zhou, *J. Mater. Chem. A*, 2013, **1**, 5301-5308.

47. D. Wang, I. Belharouak, G. Zhou and K. Amine, *Adv. Funct. Mater.*, 2013, **23**, 1070-1075.

48. H. J. Noh, J. W. Ju and Y. K. Sun, *ChemSusChem*, 2014, **7**, 245-252.

49. H. J. Noh, Z. Chen, C. S. Yoon, J. Lu, K. Amine and Y. K. Sun, *Chem. Mater.*, 2013, **25**, 2109-2115.

50. Y. K. Sun, Z. H. Chen, H. J. Noh, D. J. Lee, H. G. Jung, Y. Ren, S. Wang, C. S. Yoon, S. T. Myung and K. Amine, *Nat. Mater.*, 2012, **11**, 942-947.

51. A. Van der Ven and G. Ceder, *Electrochem. Solid-State Lett.* 2000, **3**, 301-304.

52. A. Van der Ven and G. Ceder, *J. Power. Sources,* 2001, **97-98**, 529-531.

53. K. S. Kang, Y. S. Meng, J. Breger, C. P. Grey and G. Ceder, *Science*, 2006, **311**, 977-980.

54. Y. Wang, K. Takahashi, K. Lee and G. Z. Cao, *Adv. Funct. Mater.*, 2006, **16**, 1133-1144.

55. J. X. Wang, C. J. Curtis, D. L. Schulz and J. G. Zhang, *J. Electrochem. Soc.*, 2004, **151**, A1-A7.

56. K. West, B. Zachauchristiansen, T. Jacobsen and S. Skaarup, *J. Power Sources*, 1993, **43**, 127-134.

57. A. K. Padhi, K. S. Nanjundaswamy and J. B. Goodenough, *J. Electrochem. Soc.*, 1997, **144**, 1188-1194.

58. F. Yu, L. L. Zhang, M. Y. Zhu, Y. X. An, L. L. Xia, X. G. Wang and B. Dai, *Nano Energy*, 2014, **3**, 64-79.

59. L. Dimesso, C. Forster, W. Jaegermann, J. P. Khanderi, H. Tempel, A. Popp, J. Engstler, J. J. Schneider, A. Sarapulova, D. Mikhailova, L. A. Schmitt, S. Oswald and H. Ehrenberg, *Chem. Soc. Rev.*, 2012, **41**, 5068-5080.

60. Z. H. Chen, Y. Ren, Y. Qin, H. M. Wu, S. Q. Ma, J. G. Ren, X. M. He, Y. K. Sun and K. Amine, *J. Mater. Chem.*, 2011, **21**, 5604-5609.

61. B. Kang and G. Ceder, *Nature*, 2009, **458**, 190-193.

62. D. Morgan, A. Van der Ven and G. Ceder, *Electrochem. Solid-State Lett.*, 2004, **7**, A30-A32.

63. C. A. J. Fisher and M. S. Islam, *J. Mater. Chem.*, 2008, **18**, 1209-1215.

64. M. S. Islam, D. J. Driscoll, C. A. J. Fisher and P. R. Slater, *Chem. Mater.*, 2006, **17**, 5085-5092.

65. L. Wang, F. Zhou, Y. Meng and G. Ceder, *Phys. Rev. B*, 2007, **76,** 165435.

66. B. Ellis, L. K. Perry, D. H. Ryan and L. F. Nazar, *J. Am. Chem. Soc.*, 2006, **128**, 11416-11422.

67. R. Amin, P. Balaya and J. Maier, *Electrochem. Solid-State Lett.*, 2007, **10**, A13-A16.

68. L. Wang, X. M. He, W. T. Sun, J. L. Wang, Y. D. Li and S. S. Fan, *Nano Lett.*, 2012, **12**, 5632-5636.

69. B. Pei, H. Yao, W. Zhang and Z. Yang, *J. Power Sources*, 2012, **220**, 317-323.

70. C. C. Huang, D. S. Ai, L. Wang and X. M. He, *Chem. Lett.*, 2013, **42**, 1191-1193.

71. G. B. Zeng, R. Caputo, D. Carriazo, L. Luo and M. Niederberger, *Chem. Mater.*, 2013, **25**, 3399-3407.

72. Y. Wu, Z. Wen and J. Li, *Adv. Mater.*, 2011, **23**, 1126-1129.

73. J. Jiang, W. Liu, J. Chen and Y. Hou, *ACS Appl. Mater. Interfaces.*, 2012, **4**, 3062-3068.

74. D. Rangappa, K. Sone, M. Ichihara, T. Kudo and I. Honma, Chem. Commun., 2010, **46**, 7548-7550.

75. K. Saravanan, P. Balaya, M. V. Reddy, B. V. R. Chowdari and J. J. Vittal, *Energy Environ. Sci.*, 2010, **3**, 457-464.

76. C. Nan, J. Lu, C. Chen, Q. Peng and Y. Li, *J. Mater. Chem.*, 2011, **21**, 9994-9996.

77. J. Song, L. Wang, G. Shao, M. Shi, Z. Ma, G. Wang, W. Song, S. Liu and C. Wang, *Phys. Chem. Chem. Phys.*, 2014, **16**, 7728-7733.

78. C. Nan, J. Lu, L. Li, L. Li, Q. Peng and Y. Li, *Nano Res.*, 2013, **6**, 469-477.

79. Y. Long, Y. Shu, X. Ma and M. Ye, *Electrochim. Acta*, 2014, **117**, 105-112.

80. S. H. Lim, C. S. Yoon and J. Cho, *Chem. Mater.*, 2008, **20**, 4560-4564.

81. G. Wang, X. Shen and J. Yao, *J. Power Sources*, 2009, **189**, 543-546.

82. Z. X. Dong, S. J. Kennedy and Y. Q. Wu, *J. Power Sources*, 2011, **196**, 4886-4904.

83. S. Cavaliere, S. Subianto, I. Savych, D. J. Jones and J. Roziere, *Energy Environ. Sci.*, 2011, **4**, 4761-4785.

84. E. Hosono, Y. Wang, N. Kida, M. Enomoto, N. Kojima, M. Okubo, H. Matsuda, Y. Saito, T. Kudo, I. Honma and H. Zhou, *ACS Appl. Mater. Interfaces*, 2010, **2**, 212-218.

85. C. Zhu, Y. Yu, L. Gu, K. Weichert and J. Maier, *Angew. Chem., Int. Ed.*, 2011, **50**, 6278-6282.

86. H. Xia, Z. T. Luo and J. P. Xie, *Progress in Nat. Sci.-Mater. Int.*, 2012, **22**, 572-584.

87. E. Hosono, T. Kudo, I. Honma, H. Matsuda and H. S. Zhou, *Nano Lett.*, 2009, **9**, 1045-1051.

88. M. Hirayama, H. Ido, K. Kim, W. Cho, K. Tamura, J. Mizuki and R. Kanno, *J. Am. Chem. Soc.*, 2010, **132**, 15268-15276.

89. S. Lee, Y. Cho, H. K. Song, K. T. Lee and J. Cho, *Angew. Chem., Int. Ed.*, 2012, **51**, 8748-8752.

90. Y. L. Ding, J. Xie, G. S. Cao, T. J. Zhu, H. M. Yu and X. B. Zhao, *Adv. Funct. Mater.*, 2010, **21**, 348-355.

91. D. K. Kim, P. Muralidharan, H. W. Lee, R. Ruffo, Y. Yang, C. K. Chan, H. Peng, R. A. Huggins and Y. Cui, *Nano Lett.*, 2008, **8**, 3948-3952.

92. D. Zhan, Q. Zhang, X. Hu, G. Zhu and T. Peng, *Solid State Ionics*, 2013, **239**, 8-14.

93. E. Hosono, T. Kudo, I. Honma, H. Matsuda and H. Zhou, *Nano Lett.*, 2009, **9**, 1045-1051.

94. W. Sun, F. Cao, Y. Liu, X. Zhao, X. Liu and J. Yuan, *J. Mater. Chem.*, 2012, **22**, 20952-20957.

95. J. S. Kim, K. Kim, W. Cho, W. H. Shin, R. Kanno and J. W. Choi, *Nano Lett.*, 2012, **12**, 6358-6365.

96. J. Xiao, X. L. Chen, P. V. Sushko, M. L. Sushko, L. Kovarik, J. J. Feng, Z. Q. Deng, J. M. Zheng, G. L. Graff, Z. M. Nie, D. W. Choi, J. Liu, J. G. Zhang and M. S. Whittingham, *Adv. Mater.*, 2012, **24**, 2109-2116.

97. L. Zhou, D. Y. Zhao and X. W. Lou, *Angew. Chem., Int. Ed.*, 2012, **51**, 239-241.

98. J. M. Zheng, J. Xiao, X. Q. Yu, L. Kovarik, M. Gu, F. Omenya, X. L. Chen, X. Q. Yang, J. Liu, G. L. Graff, M. S. Whittingham and J. G. Zhang, *Phys. Chem. Chem. Phys.*, 2012, **14**, 13515-13521.

99. X. L. Zhang, F. Y. Cheng, K. Zhang, Y. L. Liang, S. Q. Yang, J. Liang and J. Chen, *Rsc Adv.*, 2012, **2**, 5669-5675.

100. K. R. Chemelewski, E.S. Lee, W. Li and A. Manthiram, *Chem. Mater.*, 2013, **25**, 2890-2897.

101. B. Hai, A. K. Shukla, H. Duncan and G. Chen, *J. Mater. Chem. A*, 2013, **1**, 759-769.

102. Y. Yang, G. Zheng and Y. Cui, *Chem. Soc. Rev.*, 2013, **42**, 3018-3032.

103. D. W. Wang, Q. Zeng, G. Zhou, L. Yin, F. Li, H.M. Cheng, I. R. Gentle and G. Q. M. Lu, *J. Mater. Chem. A*, 2013, 1, 9382-9394.

104. S. Evers and L. F. Nazar, *Acc. Chem. Res.*, 2013, **46**, 1135-1143.

105. A. Manthiram, Y. Z. Fu and Y. S. Su, *Acc. Chem. Res.*, 2013, **46**, 1125-1134.

106. Y. Diao, K. Xie, X. B. Hong and S. Z. Xiong, *Acta Chimica Sinica*, 2013, **71**, 508-518.

107. Z. D. Yao, W. Wei, J. L. Wang, J. Yang and Y. N. Nuli, *Acta Physico-Chimica Sinica*, 2011, **27**, 1005-1016.

108. Y. X. Yin, S. Xin, Y. G. Guo and L. J. Wan, *Angew. Chem., Int. Ed.*, 2013, **52**, 13186-13200.

109. D. Bresser, S. Passerini and B. Scrosati, *Chem. Commun.*, 2013, **49**, 10545-10562.

110. Y. Yang, G. Y. Zheng and Y. Cui, *Chem. Soc. Rev.*, 2013, **42**, 3018-3032.

111. Z. Y. Cao and B. Q. Wei, *Energy Environ. Sci.*, 2013, **6**, 3183-3201.

112. C. H. Xu, B. H. Xu, Y. Gu, Z. G. Xiong, J. Sun and X. S. Zhao, *Energy Environ. Sci*, 2013, **6**, 1388-1414.

113. G. M. Zhou, F. Li and H. M. Cheng, *Energy Environ. Sci*, 2014, **7**, 1307-1338.

114. N. Liu, W. Y. Li, M. Pasta and Y. Cui, *Front. Phys.*, 2014, **9**, 323-350.

115. A. Fedorkova, R. Orinakova, O. Cech and M. Sedlarikova, *Int. J. Electrochem. Sci.*, 2013, **8**, 10308-10319.

116. K. Zhang, Z. Hu and J. Chen, *J. Energy Chem.*, 2013, **22**, 214-225.

117. J. J. Hu, G. R. Li and X. P. Gao, *J. Inorg. Mater.*, 2013, **28**, 1181-1186.

118. L. B. Chen, M. Zhang and W. F. Wei, *J. Nanomater.*, 2013, **940389**.

119. M. Barghamadi, A. Kapoor and C. Wen, *J. Electrochem. Soc.*, 2013, **160**, A1256-A1263.

120. S. L. Candelaria, Y. Y. Shao, W. Zhou, X. L. Li, J. Xiao, J. G. Zhang, Y. Wang, J. Liu, J. H. Li and G. Z. Cao, *Nano Energy*, 2012, **1**, 195-220.

121. J. Wang, H. L. L. Xin and D. L. Wang, *Part. Part. Syst. Char.,* 2014, **31**, 515-539.

122. A. Kausar, S. Zulfiqar and M. I. Sarwar, *Polymer Rev.*, 2014, **54**, 185-267.

123. S. Li, M. Xie, J. B. Liu, H. Wang and H. Yan, *Electrochem. Solid-State Lett.*, 2011, 14, A105-A107.

124. S. Evers and L. F. Nazar, *Chem. Commun.*, 2012, **48**, 1233-1235.

125. H. L. Wang, Y. Yang, Y. Y. Liang, J. T. Robinson, Y. G. Li, A. Jackson, Y. Cui and H. J. Dai, *Nano Lett.*, 2011, **11**, 2644-2647.

126. Y. S. Su and A. Manthiram, *Electrochim. Acta*, 2012, **77**, 272-278.

127. M. S. Park, J. S. Yu, K. J. Kim, G. Jeong, J. H. Kim, Y. N. Jo, U. Hwang, S. Kang, T. Woo and Y. J. Kim, *Phys. Chem. Chem. Phys.*, 2012, **14**, 6796-6804.

128. F. F. Zhang, X. B. Zhang, Y. H. Dong and L. M. Wang, *J. Mater. Chem.*, 2012, **22**, 11452-11454.

129. G. Zhou, S. Pei, L. Li, D. W. Wang, S. Wang, K. Huang, L. C. Yin, F. Li and H. M. Cheng, *Adv. Mater.*, 2014, **26**, 625-631.

130. Y. L. Cao, X. L. Li, I. A. Aksay, J. Lemmon, Z. M. Nie, Z. G. Yang and J. Liu, *Phys. Chem. Chem. Phy*, 2011, **13**, 7660-7665.

131. N. W. Li, M. B. Zheng, H. L. Lu, Z. B. Hu, C. F. Shen, X. F. Chang, G. B. Ji, J. M. Cao and Y. Shi, *Chem. Commun.*, 2012, **48**, 4106-4108.

132. B. Wang, K. F. Li, D. W. Su, H. J. Ahn and G. X. Wang, *Chem. Asian. J.*, 2012, **7**, 1637-1643.

133. L. Q. Lu, L. J. Lu and Y. Wang, *J. Mater. Chem. A*, 2013, **1**, 9173-9181.

134 J. Z. Wang, L. Lu, M. Choucair, J. A. Stride, X. Xu and H. K. Liu, *J. Power Sources*, 2011, **196**, 7030-7034.

135. Y. X. Wang, L. Huang, L. C. Sun, S. Y. Xie, G. L. Xu, S. R. Chen, Y. F. Xu, J. T. Li, S. L. Chou, S. X. Dou and S. G. Sun, *J. Mater. Chem.*, 2012, **22**, 4744-4750.

136. L. W. Ji, M. M. Rao, H. M. Zheng, L. Zhang, Y. C. Li, W. H. Duan, J. H. Guo, E. J. Cairns and Y. G. Zhang, *J. Am. Chem. Soc.*, 2011, **133**, 18522-18525.

137. H. Sun, G. L. Xu, Y. F. Xu, S. G. Sun, X. F. Zhang, Y. C. Qiu and S. H. Yang, *Nano Res.*, 2012, **5**, 726-738.

138. G. M. Zhou, L. C. Yin, D. W. Wang, L. Li, S. F. Pei, I. R. Gentle, F. Li and H. M. Cheng, *Acs Nano*, 2013, **7**, 5367-5375.

139. W. D. Zhou, H. Chen, Y. C. Yu, D. L. Wang, Z. M. Cui, F. J. DiSalvo and H. D. Abruna, *Acs Nano*, 2013, **7**, 8801-8808.

140. T. Q. Lin, Y. F. Tang, Y. M. Wang, H. Bi, Z. Q. Liu, F. Q. Huang, X. M. Xie and M. H. Jiang, *Energy Environ. Sci.*, 2013, **6**, 1283-1290.

141. W. C. Peng and X. Y. Li, *Nano Res.*, 2013, **6**, 286-292.

142. M. Xiao, M. Huang, S. S. Zeng, D. M. Han, S. J. Wang, L. Y. Sun and Y. Z. Meng, *Rsc Adv.*, 2013, **3**, 4914-4916.

143. B. Zhang, X. Qin, G. R. Li and X. P. Gao, *Energy Environ. Sci.*, 2010, **3**, 1531-1537.

144. G. Xu, B. Ding, L. Shen, P. Nie, J. Han and X. Zhang, *J. Mater. Chem. A*, 2013, **1**, 4490-4496.

145. H. B. Wu, S. Wei, L. Zhang, R. Xu, H. H. Hng and X. W. Lou, *Chem. Eur. J.*, 2013, **19**, 10804-10808.

146. A. Walcarius, *Chem. Soc. Rev.*, 2013, **42**, 4098-4140.

147. Y. Ren, Z. Ma and P. G. Bruce, *Chem. Soc. Rev.*, 2012, **41**, 4909-4927.

148. X. L. Ji, K. T. Lee and L. F. Nazar, *Nat. Mater.*, 2009, **8**, 500-506.

149. S. R. Chen, Y. P. Zhai, G. L. Xu, Y. X. Jiang, D. Y. Zhao, J. T. Li, L. Huang and S. G. Sun, *Electrochim. Acta*, 2011, **56**, 9549-9555.

150. J. Schuster, G. He, B. Mandlmeier, T. Yim, K. T. Lee, T. Bein and L. F. Nazar, *Angew. Chem., Int. Ed.*, 2012, **51**, 3591-3595.

151. C. D. Liang, N. J. Dudney and J. Y. Howe, *Chem. Mater.*, 2009, **21**, 4724-4730.

152. X. L. Li, Y. L. Cao, W. Qi, L. V. Saraf, J. Xiao, Z. M. Nie, J. Mietek, J. G. Zhang, B. Schwenzer and J. Liu, *J. Mater. Chem.*, 2011, **21**, 16603-16610.

153. S. Xin, L. Gu, N. H. Zhao, Y. X. Yin, L. J. Zhou, Y. G. Guo and L. J. Wan, *J. Am. Chem. Soc.*, 2012, **134**, 18510-18513.

154. D. L. Wang, Y. C. Yu, W. D. Zhou, H. Chen, F. J. DiSalvo, D. A. Muller and H. D. Abruna, *Phys. Chem. Chem. Phy*, 2013, **15**, 9051-9057.

155. X. Zhou, J. Xie, J. Yang, Y. Zou, J. Tang, S. Wang, L. Ma and Q. Liao, *J. Power Sources*, 2013, **243**, 993-1000.

156. X. Y. Zhao, J. P. Tu, Y. Lu, J. B. Cai, Y. J. Zhang, X. L. Wang and C. D. Gu, *Electrochim. Acta*, 2013, **113**, 256-262.

157. W. Bao, Z. Zhang, W. Chen, C. Zhou, Y. Lai and J. Li, *Electrochim. Acta*, 2014, **127**, 342-348.

158. T. Xu, J. X. Song, M. L. Gordin, H. S. Sohn, Z. X. Yu, S. R. Chen and D. H. Wang, *ACS Appl. Mater. Interfaces*, 2013, **5**, 11355-11362.

159. G. Ma, Z. Wen, J. Jin, Y. Lu, K. Rui, X. Wu, M. Wu and J. Zhang, *J. Power Sources*, 2014, **254**, 353-359.

160. J. Jin, Z. Wen, G. Ma, Y. Lu and K. Rui, *Solid State Ionics*, 2014, **262**, 170-173.

161. D. Li, F. Han, S. Wang, F. Cheng, Q. Sun and W. C. Li, *ACS Appl. Mater. Interfaces*, 2013, **5**, 2208-2213.

162. G. L. Xu, Y. F. Xu, J. C. Fang, X. X. Peng, F. Fu, L. Huang, J. T. Li and S. G. Sun, *ACS Appl. Mater. Interfaces*, 2013, **5**, 10782-10793.

163. H. Xu, Y. Deng, Z. Shi, Y. Qian, Y. Meng and G. Chen, *J. Mater. Chem. A*, 2013, **1**, 15142-15149.

164. C. Wang, K. Su, W. Wan, H. Guo, H. Zhou, J. Chen, X. Zhang and Y. Huang, *J. Mater. Chem. A*, 2014, **2**, 5018-5023.

165. H. Zhao, Z. Peng, W. Wang, X. Chen, J. Fang and J. Xu, *J. Power Sources*, 2014, **245**, 529-536.

166. X. B. Cheng, J. Q. Huang, Q. Zhang, H. J. Peng, M. Q. Zhao and F. Wei, *Nano Energy*, 2014, **4**, 65-72.